Nano-particle mediated M2 macrophage polarization enhances bone formation and MSC osteogenesis in an IL-10 dependent manner

Olwyn R. Mahon[a,c], David C. Browe[c,d], Tomas Gonzalez-Fernandez[c,d,e], Pierluca Pitacco[c,d], Ian T. Whelan[c,d,g], Stanislas Von Euw [c,d], Christopher Hobbs[e,f], Valeria Nicolosi[e,f], Kyle T. Cunningham[a], Kingston. H. G. Mills[a], Daniel J. Kelly[c,d,e,g *§] and Aisling Dunne[a,b*§]

[a] School of Biochemistry and Immunology, Trinity College Dublin, Dublin, Ireland.
[b] School of Medicine, Trinity College Dublin, Dublin, Ireland.
[c] Trinity Centre for Bioengineering, Trinity Biomedical Sciences Institute, Trinity College Dublin, Dublin, Ireland.
[d] Department of Mechanical and Manufacturing Engineering, School of Engineering, Trinity College Dublin, Dublin, Ireland.
[e] Advanced Materials and Bioengineering Research (AMBER) Centre, Trinity College Dublin, Ireland
[f] Centre for Research on Adaptive Nanostructures and Nanodevices (CRANN), Trinity College Dublin, Ireland; AMBER Centre, Trinity College Dublin, Ireland.
[g] CÚRAM Center for Research in Medical Devices, National University of Ireland, Galway, Ireland

* These authors contributed equally.
§ Corresponding authors at: aidunne@tcd.ie; kellyd9@tcd.ie

Abstract

Engineering a pro-regenerative immune response following scaffold implantation is integral to functional tissue regeneration. The immune response to implanted biomaterials is determined by multiple factors, including biophysical cues such as material stiffness, topography and particle size. In this study we developed an immune modulating scaffold for bone defect healing containing bone mimetic nano hydroxyapatite particles (BMnP). We first demonstrate that, in contrast to commercially available micron-sized hydroxyapatite particles, in-house generated BMnP preferentially polarize human macrophages towards an M2 phenotype, activate the transcription factor cMaf and specifically enhance production of the anti-inflammatory cytokine, IL-10. Furthermore, nano-particle treated macrophages enhance mesenchymal stem cell (MSC) osteogenesis *in vitro* and this occurs in an IL-10 dependent manner, demonstrating a direct pro-osteogenic role for this cytokine. BMnPs were also capable of driving pro-angiogenic responses in human macrophages and HUVECs. Characterization of immune cell subsets following incorporation of functionalized scaffolds into a rat femoral defect model revealed a similar profile, with micron-sized hydroxyapatite functionalized scaffolds eliciting pro-inflammatory responses characterized by infiltrating T cells and elevated expression of M1 macrophages markers compared to BMnP functionalized scaffolds which promoted M2 macrophage polarization, tissue vascularization and increased bone volume. Taken together these results demonstrate that nano-sized Hydroxyapatite has immunomodulatory potential and is capable of directing anti-inflammatory innate immune-mediated responses that are associated with tissue repair and regeneration.

Keywords: Macrophage polarization, Immune response, Hydroxyapatite, nano-particle, bone-mimietic, IL-10, Osteogenesis, bone regeneration.

Introduction

The field of tissue engineering has placed significant focus on designing biomaterial scaffolds capable of directing the fate of tissue-specific progenitor cells. A number of studies have demonstrated that the specific composition of engineered constructs can impact MSC differentiation and that properties inherent to biomaterials such as topography and stiffness can direct lineage specific cell differentiation and promote successful tissue integration *(1–4)*. In addition to scaffold composition, efforts are being made to manipulate the interplay between MSCs and the host immune system given that innate immune cells, including macrophages, will interact will tissue specific progenitor cells to direct tissue regeneration *(5)*. Despite the fact that promoting an appropriate immune response is integral to the success of any implant *(6)*, there has been less focus on the design of scaffolds capable of eliciting immune responses that specifically direct functional tissue regeneration.

While it is well accepted that an early inflammatory response is required to initiate pro-regenerative responses post-injury, a shift from pro-inflammatory to anti-inflammatory function is required to maximize the regenerative capacity of progenitor cells and minimize the destructive effects of prolonged inflammation. In the field of bone regeneration, it has been demonstrated that administration of pro-inflammatory cytokines, such as TNFα to fracture sites immediately after injury accelerates fracture repair *(7)*, while prolonged administration inhibits cartilage formation in the early phase of bone induction *(8)*. The temporal nature of the inflammatory responses is largely attributed to the transition of macrophages form a classically activated ‘M1’ state, which play a role in early angiogenesis, to alternatively activated ‘M2’ macrophages, which promote

ECM synthesis, vessel formation and osteogenic differentiation. Scaffolds loaded with IFNγ and IL-4 to promote sequential polarization of M1 and M2 macrophages, respectively, have shown promising results in fracture repair models, further attesting to the contribution of innate immune cells in bone reconstitution *(9)*. The contribution of the adaptive immune system to bone healing has also been explored using RAG knockout mice and the results indicated that functional T and B cell responses decelerate bone repair *(10)*. Overall, these studies provide compelling evidence that modulation of immune responses may serve as a beneficial strategy to consider when designing scaffolds for efficient osteoinduction.

The size and morphology of biomaterials used to functionalize scaffolds can also impact MSC fate and both micron-sized hydroxyapatite (HA) and nano-sized HA have received significant attention in this regard due to their inherent osteoconductive and osteoinductive capabilities *(11)*. We have recently reported that micron-sized HA particles promote M1 macrophage polarization in primary human macrophages and have identified the specific signaling pathways involved in driving activation of M1 macrophages *(12)*. The direct impact of nano-sized HA particles on macrophage phenotype has not yet been addressed, nor has the influence of HA-dependent macrophage phenotype on MSC differentiation. Here we demonstrate that nanoHA particles, which we term bone mimetic nanoparticles (BMnP) due to their chemical and physical similarity to natural bone, have potent immunomodulatory properties and are capable of promoting M2 macrophage polarization both *in vitro* and *in vivo* when incorporated into functionalized extracellular matrix (ECM)-based scaffolds. Furthermore, we have identified IL-10 as a key cytokine driving osteogenic differentiation of MSCs in response to BMnP-stimulated macrophages, demonstrating a direct pro-osteogenic role for this cytokine. New approaches being explored to improve biomaterial integration and tissue regeneration include the incorporation of

immune modulating cytokines into tissue engineering scaffolds *(13–15)* however, the data presented here provides compelling evidence that biomaterial particles themselves can direct immune-mediated responses associated with tissue repair and regeneration.

Materials and Methods

Study design

This study was designed to examine the role of particle size on human macrophage phenotype and stem cell osteogenesis. The use of human blood samples for this study was approved by the research ethics committee of the School of Biochemistry and Immunology, Trinity College Dublin and was conducted in accordance with the Declaration of Helsinki. Leukocyte-enriched buffy coats from anonymous healthy donors were obtained with permission from the Irish Blood Transfusion Service (IBTS), St. James's Hospital, Dublin. Donors provided informed written consent to the IBTS for their blood to be used for research purposes. All animal experiments were conducted in accordance with the recommendations and guidelines of The Health Products Regulatory Authority, the competent authority in Ireland responsible for the implementation of Directive 2010/63/EU on the protection of animals used for scientific purposes in accordance with the requirements of the Statutory Instrument No. 543 of 2012. Animal experiments were carried out under license (AE 19136/P039) approved by The Health Products Regulatory Authority and in accordance with protocols approved by Trinity College Dublin Animal Research Ethics Committee. The *n* for rodent models was based on the predicted variance in the model and was powered to detect 0.05 significance. Animals were randomly assigned to experimental groups before surgical procedure.

Preparation of micron and nano particle suspensions

1) Synthesis of nanoHydroxyapatite particles (BMnP)

Bone mimetic nano-sized Hydroxyapatite particles were prepared following a previously described protocol *(16)*. Briefly, a solution of 20 mM calcium chloride was added to a solution of 12 mM sodium phosphate, containing 0.017% DARVAN 821A (RT Vanderbilt) as the dispersant, and nanoHydroxyapatite particles were precipitated. This solution was centrifuged, reconstituted in endotoxin-free water and filtered through a 0.2 μm filter to remove aggregated particles.

2) Preparation of micron Hydroxyapatite particle suspension

Commercial micron HA particles ($Ca_5(OH)(PO_4)_3$ [18-20]were purchased from Sigma Aldrich (Cat# 04238), weighed out and resuspended at a concentration of 5 mg/ml in endotoxin-free water, sonicated for 10 min and stored at 4°C.

Particle sized determination

Particle size distributions of micron sized HA particles and nanoHA particles were measured using dynamic light scattering (DLS) (ZetaSizer 3000 HS, Malvern instruments, UK). Measurements were carried out under monochromatic, coherent He-Ne laser light of fixed wavelength (633nm) at room temperature with each size determination yielding an average particle size expressed as the mean diameter (Z_{ave}) together with a graph of the size range.

Structural and Physical characterization of Particles

Powder X-ray diffraction (XRD) analysis was performed in a Bruker D8 Discover diffractometer operating in the reflection mode at CuKα radiation of wavelength 0.154 nm and 2Θ values from 10° to 60°, using a step scan of 0.02°/step and held for 2s/step. The Fourier-transform infrared

(FTIR) spectroscopy experiments from powdered samples were conducted with a SpectrumOne (Perkin–Elmer) spectrometer in attenuated total reflection (ATR) mode. The spectra were recorded by accumulating 16 scans in the range of 650–4000 cm^{-1} at a resolution of 4 cm^{-1}. The solid-state Nuclear Magnetic Resonance (NMR) spectroscopy experiments were conducted on a Bruker 400 MHz Avance-III spectrometer running TopSpin software. Powdered samples were packed into 4.0 mm (o.d.) zirconia rotors and spun at 20 kHz in a 4 mm Bruker MAS probe. ^{1}H chemical shifts were referenced to TetraMethylSilane (TMS) at $\delta^{1}H$ = 0.0 ppm, while ^{31}P chemical shifts were referenced to H_3PO_4 (85% w/w aqueous solution) at $\delta^{31}P$ = 0.0 ppm. To allow full relaxation of the magnetization, ^{1}H recycle delays were set to 2s and 20s for nano and micron HA, respectively; whereas ^{31}P recycle delays were set to 240s and 300s for nano and micron particles, respectively. In the two-dimensional (2D) $\{^{1}H\}^{31}P$ Heteronuclear Correlation (HetCor) MAS NMR spectra, the ^{1}H relaxation delays were set to 2s and 4s for nano and micron particles, respectively; the contact time (t_{CP}) was set to 1ms for both particle sizes; and 128 scans were accumulated for each 256 t1 increments.

Micron particle size and morphology was characterized using scanning electron microscopy. Scanning Electron Microscopy (SEM) was carried out on an ULTRA Plus microscope (Zeiss, Oberkochen, Germany) operating at 5 kV acceleration voltage. The micron HA sample was deposited on an aluminum stud using conductive carbon adhesive stickers and was subsequently coated with approximately 5 nm of Au/Pd prior to imaging. Nanoparticle size and morphology was characterized by transmission electron microscopy (TEM). Samples were prepared by placing approximately 5 µl onto a lacey carbon film Cu TEM grid (Agar Scientific, UK) and allowed to air dry overnight. Samples were imaged using a Titan TEM (ThermoFisher Scientific, Eindhoven, The Netherlands) at 300 kV.

Assessment of endotoxin contamination

In-house synthesized nanoparticles and micron HA particles (Sigma Aldrich (Cat# 04238)) were first tested for lipopolysaccharide (LPS) contamination using the HEK-Blue^{TM} hTLR4 assay system (Invivogen). HEK-blue cells (5 x 10^5 cells/ml) expressing TLR4 were stimulated with LPS (10–100 ng/ml; positive control), micron or nano HA particles (250 mg/ml) for 24 h. The expression of SEAP which is under the control of NF-κB and AP-1 was tested by incubating cell supernatants with HEK-blue detection medium for 30 min at 37 °C and absorbance was read at 650 nm.

Human blood monocyte-derived macrophage isolation

Peripheral blood mononuclear cells (PBMC) were isolated by density gradient centrifugation from leukocyte-enriched buffy coats from anonymous healthy donors, obtained with permission from the Irish Blood Transfusion Board, St. James's Hospital, Dublin. $CD14^+$ cells were positively selected using antiCD14 magnetic beads (Miltenyi Biotech, Germany) and shown to be >90% pure, as determined by flow cytometry. Cells were cultured at 1 x 10^6 cells/ml for 6 days in RPMI 1640 medium supplemented with 1% penicillin-streptomycin and 10% Foetal Bovine Serum. Macrophage were differentiated by adding M-CSF (50 ng/ml) to the cultures on days 0 and 3. >95% of cells were $CD14^+CD11b^+$ as determined by flow cytometry. All media was removed on day 7 and replaced with fresh media for experimental treatments to ensure no residual M-CSF would interfere with experimental treatment groups.

Isolation and expansion of human bone marrow-derived MSCs

Bone marrow aspirates (Lonza) were washed in PBS and centrifuged at 900g for 10 mins, supernatant was gently aspirated and cells were plated at 40-60 x 10^6/T175 (4000-5000 MSCs/cm^2 in complete media (DMEM, 10% FBS, 1% P/S, 5ng/ml bFGF2). Cells were cultured for up to two weeks (until colonies form and cells proliferate), with media being replenished every 3-4 days. Cells were washed with PBS in between feedings to dislodge red blood cells. Adherent cells were expanded up to P2 and were characterized by their plastic adherence and fibroblastic nature. Colony Forming Unit assays were used to quantify proliferation, and Trilineage Potential assays were used to determine pluripotency. For *in vitro* assays, MSCs were seeded at 5 x 10^4 cells/ml in cDMEM.

Macrophage conditioned media experiment

Primary human macrophages were cultured with 250μg/ml of micron or nano particles for 24 hours. The conditioned media (CM) collected from treated macrophages was centrifuged for 1 hour at 300 x g to remove any residual The quantity of calcium in the media before and after centrifugation was assessed using the o-cresolphthalein complexone method (Stanbio calcium kit) and compared to control media. Results confirm that calcium levels post-centrifugation are comparable to that of control media. (Supplementary Fig. 1). Human MSCs were cultured in the CM for 48 hours and then cultured for a further 7 days in osteogenic media (DMEM + GlutaMAX media supplemented with 100mM dexamethasone, 10mM β-Glycerolphosphate, and 0.05mM L-ascorbic acid-2-phosphate).

IL-10 neutralization experiment

For neutralization of IL-10 in macrophage culture, cells were pre-treated with an IL-10 neutralizing antibody (MAB217 from R&D) at 2 µg/ml for 30 minutes. Cells were then treated with particles (250 µg/ml) for 24 hours.

For neutralizing of IL-10 in the MSC culture, macrophages were stimulated with particles (250 µg/ml) for 24 hours. Conditioned media was collected, centrifugated to deplete of residual particles and incubated for 30 minutes with anti-IL-10 (2 µg/ml) to allow the antibody to bind to IL-10 in the media. Media was then placed onto MSCs for 48 hours.

Alizarin Red staining

To evaluate calcium deposition, MSCs in monolayer cultured for 7 days were stained with 1% alizarin red solution (AR). Cell culture supernatants were removed and cells were rinsed with PBS prior to being fixed in 100% ethanol for 10 minutes at room temperature. This was removed and cells were rinsed again with PBS prior to the addition of 1% AR. AR was removed after 2 minutes, cells were washed with deionized water and fixed again with 100 % ethanol. Stained samples were air dried and images were captured using phase transmission microscope (Olympus, UK). Semi-quantitative analysis of AR staining was performed through extraction of the dye using 10% cetylpyridinium chloride and measuring the absorbance at 540 nm.

Wound scratch assay

MSCs were seeded onto 6 well plates and grown to confluence prior to being serum starved for 16 hours. A single scratch wound was induced through the middle of each well with a sterile pipette

tip, cells were washed with media to remove lifted cells and media was replaced fresh serum free media. Cells were subsequently either left in serum free control media or cultured in serum free media from untreated, micron or nanoparticle treated macrophages for 24 hours. MSC migration across the wound margins from 24 hours was assessed and photographed using a phase-contrast microscope (Olympus 1X83). Semi-quantitative analysis of cell repopulation of the wound was assessed by three blinded observers. Tiff images of the scratch wound assays were taken at × 20 magnification at 0 and 24 hours. The mean number of cells that migrated back into the wound was calculated from six individual measurements for each wound at each time point. This process was carried out for all biological repeats. Total numbers of cells were also counted in each group to assess for proliferation.

HUVEC Tube Formation

Matrigel (100 µl; BD Biosciences, San Jose, CA, USA) was plated in 48-well culture plates after thawing on ice and allowed to polymerise for 45 min at 37°C in humidified air with 5% CO_2. HUVECs (2×10^4) were plated in serum-free Microvascular Endothelial Cell Growth Medium-2 (Lonza) without or with VEGF (10 ng/ml) as negative and positive controls respectively. Alternatively, cells were seeded in 50% supplemented serum-free conditioned media from micron or nano particle treated macrophages as previously described. Cells were imaged using phase-contrast microscopy every 2 hours to assess endothelial cell tubule formation. Average branch length, average number of branches and average number of junctions were quantified using ImageJ.

Cytokine measurements

Primary macrophages were primed with LPS (100 ng/ml) for 2 h prior to stimulation with particles (250 μg/ ml) for 24 h for inflammasome assays. Alternatively, cells were treated with particles (250 μg/ml) for 24 hours. Supernatants were harvested and cytokine concentrations of IL-1β, IL-1α (R&D Systems), TNFα, IL-6, IL-8 and IL-10 (eBiosciences) were quantified by ELISA (R&D Systems). 50-75 μl of capture antibody diluted in coating buffer was applied to high-binding 96-well plates (Greiner Bio-one). Plates were incubated overnight at 4°C, capture antibody was removed and non-specific binding sites were blocked with appropriate blocking solution (1% (w/v) BSA) for 1 hour at room temperature. After blocking, plates were washed in PBS-tween solution, dried and supernatant samples were loaded into wells in triplicates either neat or diluted 1 in 3 with assay diluent. A standard curve of serially diluted recombinant cytokine standard was also loaded onto the plates in triplicate. Blank wells, containing assay diluents only, were included on each plate to allow the subtraction of background from each sample. Samples were incubated overnight at 4°C. After washing, biotinylated detection antibody was added to each well and incubated for 2 hours at room temperature. Plates were washed and horseradish-peroxidase (HRP) conjugated to streptavidin was applied to wells for 30 minutes in the dark. Wells were thoroughly washed and the substrate, TMB or OPD, was added as required by manufacturer. The enzyme-mediated colour reaction was protected from light while developing and stopped with the addition of 1M H_2SO_4. The optical density of the colour was determined by measuring the absorbance at 450 nm using a microtiter plate reader (versamax Tunable Microplate reader (Molecular Devices). Cytokine concentrations were calculated from the standard curve using Softmax Pro software.

Real-time polymerase chain reaction (PCR)

For assessment of macrophage phenotype, cells (5 x 10^5 /well) were treated with micron or nano particles for 24 h. RNA was extracted using High Pure RNA Isolation Kits (Roche, Basel, Switzerland) and assessed for concentration and purity using the NanoDrop 2000c UVis spectrophotometer. RNA was equalized and reverse transcribed using the Applied Biosystems High-Capacity cDNA reverse transcription kit. Real-time PCR was carried out on triplicate cDNA samples with the use of the CFX96 Touch Real-Time PCR Detection System (Bio-Rad Laboratories, California). Real-time PCR for the detection of CCL19, CXCL11, CCL13 and MRC1 mRNA was performed using the TaqMan fast universal PCR Master Mix (Applied Biosystems) and predesigned TaqMan gene expression primers. mRNA amounts were normalized relative to the housekeeping gene Ribosomal Protein 18s. For assessment of osteogenic gene expression in MSCs, Sigma primers for BMP2, ALP, OPN, OCN, Runx2 and Osx (Supplementary Table 1) were used and mRNA amounts were normalized to GAPDH as housekeeping gene.

Western blotting

Primary macrophages (2 x 10^6 cells/well) were stimulated with LPS (100 ng/ml), IFN-γ (20 ng/ml), IL-4 (20 ng/ml), micron or nano sized Hydroxyapatite particles (250 μg/ml) for 24 hours for the detection of c-Maf, CD206 and CD163 protein. Cells were lysed by addition of RIPA buffer (Tris 50 mM; NaCl 150 mM; SDS 0.1%; sodium deoxycholate 0.5%; Triton X 100). Samples were subjected to SDS-PAGE (12% gel for c-Maf, 8% gel for CD206 and CD163) prior to transfer to PVDF membranes and detection with anti-c-Maf, anti-CD206 or anti-CD163 antibodies (Supplementary Table 2). For detection of Stat-3 phosphorylation, cells were stimulated with BMnPs (250 μg/ml) over the course of 60 minutes. Cells were lysed as described above with RIPA buffer containing phosphatase inhibitor cocktail 3 (Sigma-Aldrich). Samples were subjected to

SDS-PAGE (12% gel) prior to transfer to PVDF membranes and detection with anti-phospho-Stat-3 antibody (Supplementary Table 2).

Assessment of human macrophage phenotype

For flow cytometric analysis of macrophage phenotype particle-treated macrophages were Fc blocked for 15 minutes prior to staining with fluorochrome conjugated antibodies specific for CD14, CD11b, CD86 (M1), CD163 and CD206 (M2), fixed with 4% PFA washed and acquired on a FACSCanto™ II or LSRFortessa™ (both BD Biosciences) and analyzed by flow cytometry. Compensation beads singly stained with every fluor channel utilized were acquired to adjust for spectral overlap. An unstained sample was also run as a control.

For immunocytochemical analysis of macrophage phenotype, particle-treated macrophages were fixed with 4% PFA, incubated in Block and Perm solution (3% BSA with 0.1% Triton X) for 1 hour at room temperature. Cells were then incubated in primary antibodies against CD206 or CD80 (1:1000 and 1:500 dilutions respectively) overnight at 4°C. Cells were washed and incubated in secondary antibodies for 1 hour at room temperature (anti-rabbit Alexa Fluor 488 and anti-rabbit Alexa Fluor 647 for CD206 and CD80 respectively; both 1:1000). Cells were washed and counterstained with DAPI (1 ug/ml) for 15 minutes and imaged using a Leica SP8 scanning confocal microscope.

Evaluation of particle uptake

Micron and nano particles were fluorescently stained with fluorescein-5-maleimide to visualize internalization. One milligram of each particle type was suspended in 1 ml of PBS and sonicated for 5 min before adding 4 ml of fluorescein-5-maleimide stock solution (5mg/ml). The particle–

fluorescein mixture was left to react at 4 °C at 1400 rpm for 12 h. The stained particles were washed five times with PBS. Cells were incubated with tagged particles for 1 or 3 hours, fixed with 4% PFA for 10 mins, permeabilised in 0.5% Triton in PBS for 15 minutes and stained with Rhodamine red (1:2000) for 1 hour before being stained with DAPI (1:1000) for 15 minutes. Cells were imaged using a Leica SP8 scanning confocal microscope. FITC fluorescence intensity from images was quantified using Image J and is displayed as corrected total cell fluorescence (CTCF). Cells were pretreated with the actin polymerization inhibitor, Latrunculin B (1µM), for 45 minutes prior to treatment with particles for 24 hours. RNA was extracted as previously described and M1 and M2 associated genes (CXCL9, CXCL10, MRC1 and CCL13) were assessed by Real-Time PCR.

Functionalized ECM Scaffold fabrication

Articular cartilage (AC) and growth plate (GP) used in the fabrication of ECM-derived scaffolds were harvested from the femoral condyles of female pigs (4 months old) shortly after sacrifice. The cartilage was obtained using a biopsy punch (8 mm) to remove articular cartilage from the head of the femur. Following this, the head of the bone was sawed in half and hammered through the epiphyseal line to gain access to the growth plate. Tissue was pre-treated with 0.2M NaOH, digested with pepsin (1500 U/ml) and solubilised with NaCl (0.9 M for AC and 2.5 M for GP).The collagen pellet was resuspended in 0.5M acetic acid followed by rotation at 4 rpm overnight at room temperature to fully dissolve the collagen into suspension. The salt precipitation procedure was then repeated a second time. The acid solubilised collagen was dialysed against 0.02M $Na_2HPO_4$for 48 hours at 4°C before being freeze dried.

Prior to fabrication of HA functionalized scaffolds, the inherent immunomodulatory activity of AC and GP ECM was compared by culturing with primary human macrophages. Pro-

inflammatory cytokine (TNFα, IL-6 and IL-8) production was assessed by ELISA, while chemokine (CXCL10 and CXCL11) gene expression was quantified by real-time PCR. AC-ECM was deemed the least immunomodulatory of the two and was therefore selected for further scaffold fabrication. Lyophilized AC was resuspended in high glucose DMEM+Glutamax (DMEM - Gibco) to give a final concentration of 10 mg/ml. ECM slurry was mixed with either micron particles or nanoparticles at a ratio of 1:1 before chemically crosslinking using glyoxal (Sigma) at a final concentration of 10 mM for 30 mins at 37°C. The solution was then transferred to custom made moulds (height 5mm and diameter 3mm) and freeze dried (FreeZone Triad, Labconco, KC, USA). Scaffolds were subsequently physically crosslinked in a vacuum oven (VD23, Binder, Germany) by dehydrothermal (DHT) treatment at 115°C for 24 hours at 2 mBar. Scaffold pore size was determined using SEM imaging as follows: SEM images were obtained using a Zeiss Ultra Plus (Zeiss, Germany) with an acceleration voltage of 5kV and working distance of 5mm. To quantify the mean pore size of the various scaffolds, 3 images (containing a minimum of 100 pores) from 3 different scaffolds were measured using imageJ. Scaffold porosity was determined by gravimetry as previously described *(17, 18)*. Scaffolds were weighed using a digital mass balance and dimensions obtained using vernier callipers to calculate density value. Total porosity is measured by gravimetry according to the equation $(1 - \rho_{scaffold}/\rho_{material})$, where ρ=density.

Surgical procedure

Critically-sized (5 mm) femoral defects were created in immune-competent adult Fischer rats (>12 weeks old) following an established procedure *(19)*. Constructs were press-fit into the defect site, and repair tissue was harvested for analysis at 1 and 4 weeks post-implantation. One defect was created per animal and n = 5-8 constructs were implanted per time point. Briefly, anesthesia was

induced and maintained by isoflurane-oxygen throughout the surgery. The rats were also injected with buprenorphine to provide pain relief during and after surgery. The shaft of the left femur was exposed by dissections and the periosteum was scraped back to allow access to the bone. A weight-bearing polyetheretherketone (PEEK) internal fixation plate was secured to the exposed femur with four screws into pre-drilled holes. A 5 mm mid-diaphyseal defect was then created using a dental drill fitted with 2 small circular parallel saw blades welded to a narrow straight rod separated with a 5 mm spacer. The defect site was thoroughly irrigated with saline to remove bone debris before it was treated with a construct. The wounds were closed with sutures and the rats were allowed to recover. On dates of scheduled explant retrieval, rats were sacrificed by CO_2 asphyxiation. The repaired femur, with the PEEK plate fixator intact, was carefully separated from the adjacent hip and knee joints for analysis.

Characterization of immune cell subsets in rat femoral defect model

Punch biopsies (4 mm) of the defect site were performed 1 week post-surgery and cells were recovered by digestion in a Collagenase digestion cocktail (Collagenase VI (2 mg/ml), DNAse I (0.1 mg/ml) and Hyaluronidase (0.5 mg/ml) for 45 minutes at 37°C and 255 rpm. Cells were blocked by incubating in Fcγ blocker (BD Pharmingen; 1 μg/ml) for 10 min. To discriminate live from dead cells, cells were stained with LIVE/DEAD Aqua for an additional 30 min. Staining was performed with fluorescent antibodies specific CD11b (M1/70), CD3 (17A2), Ly6G (1A8), CCR2 (SA203G11), CX3CR1 (SA011F11), Ly6C (AL-21), CD19 (1D3), F4/80 (BM8), Siglec F (E50-2440), CD45 (30-F11), MHCII (M5144.15.2), and CD86 (GL-1) (Supplementary Table 3). Cells were acquired using FACS Canto II (BD), or LSRFortessa (BD). Analysis was completed using

FlowJo version 9.2 (Tree Star). Gating strategies utilised in all experiments are detailed in Supplementary Figure 2.

In order to assess circulating cytokines 1week post-surgery, cardiac punctures were performed and blood samples were centrifugated at 300 x g for 20 minutes and serum was collected. IL-10 and IFNγ cytokine concentrations were quantified by ELISA (R&D systems).

In vivo μCT analysis

μCT scans were performed on constructs using a Scanco Medical vivaCT 80 system (Scanco Medical, Bassersdorf, Switzerland). Rats (n = 8) were scanned at 4 weeks post-surgery to assess defect bridging and bone formation within the defect. First, anesthesia was induced in an induction chamber. Next, the rats were placed inside the vivaCT scanner and anesthesia was maintained by isoflurane-oxygen throughout the scan. Next, a radiographic scan of the whole animal was used to isolate the rat femur. The animal's femur was aligned parallel to the scanning field-of view to simplify the bone volume assessments. Scans were performed using a voltage of 70 kVp, and a current of 114 mA. A Gaussian filter (sigma = 0.8, support = 1) was used to suppress noise and a global threshold of 210 corresponding to a density of 399.5 mg hydroxyapatite/cm3 was applied. A voxel resolution of 35 mm was used throughout. 3D evaluation was carried out on the segmented images to determine bone volume and density and to reconstruct a 3D image. Bone volume and bone density in the defects was quantified by measuring the total quantity of mineral in the central 130 slices of the defect. The variance of bone density with depth through the constructs was analyzed qualitatively by examining sections at a depth of 25%, 50% and 75% from the top of the construct (one quarter, mid and three-quarter sections). The bone volume and densities were then quantified using scripts provided by Scanco.

Histological and immunohistochemical analysis

Constructs were fixed in 4% paraformaldehyde, dehydrated in a graded series of ethanols, embedded in paraffin wax, sectioned at 10 μm and affixed to microscope slides. Post-implantation constructs were decalcified in EDTA for 1 week. The sections were stained with haematoxylin and eosin (H&E) to assess tissue architecture and cell infiltration. Von Willibrand (vWF) and alpha smooth muscle actin (α-SMA) staining was performed by performing antigen retrieval with proteinase K solution (20 minutes at 37° C) in a humidified chamber. Slides were washed with PBS-Tween 0.5% v/v and blocked (3% donkey serum, 1% BSA in PBS) for 1 hour at room temperature. Slides were incubated in primary antibody overnight (1:250 and 1:200 dilution for α-SMA and vWF respectively), washed with 1% BSA prior to incubation with secondary antibody (both 1:200) for 1 hour. Slides were washed with 1% BSA, mounted with flouroshield mounting media, dried and imaged using a Leica SP8 scanning confocal microscope.

Statistical Analysis

A one-way ANOVA or Kruskal-Wallis test were used for the comparison of more than two groups for parametric and non-parametric analysis respectively, with the Tukey or Dunn's post-test (where applicable). A paired Student's t-test was used when there were only two groups for analysis and the data was normally distributed and a Two-tailed paired Wilcoxon Signed rank test was used for normally distributed data. All statistical analysis was performed on GraphPad Prism 7.00 (GraphPad Software). P values of <0.05 were considered significant and denoted with an asterisk. Normality tests were carried out to ensure that the data was normally distributed for parametric statistical tests.

Results

Chemical and physical characterization of micron and nano-sized Hydroxyapatite particles.

Nanohydroxyapatite particles were produced using the dispersant-aided precipitation method described previously *(16)*. These particles have previously been deemed suitable for incorporation into scaffolds for bone tissue engineering *(20)*. In order to characterize these particles in more detail, a number of physical characterization techniques were applied to analyze structural and compositional features. Commercially available micron sized HA was included for comparative purposes. Powder X-ray diffraction (XRD) analysis showed that the Bragg diffraction peaks of nanoparticles were largely broadened compared to those of micron particles indicating that the nanoparticles are a "poorly crystalline apatite", while micron particles appear as a well crystallized apatite (Fig. 1A i). Transmission electron microscopy (TEM) revealed nanoparticles were in the form of nanosized rod-like particles whose length and width range from approximately 50 to 100 nm and from 15 to 25 nm, respectively, consistent with previous reports *(16, 21)*. In contrast, scanning electron microscopy (SEM) observations show that micron particles were 1-2μM in size and irregular in shape. (Fig. 1A ii). The size of the particles was confirmed using dynamic light scattering (Supplementary Fig. 3). Analysis of the chemical composition, specifically the presence of hydroxyl (OH^-) and carbonate (CO_3^{2-}) ions and of water molecules, of both particle types was performed using Fourier-transform infrared (FTIR) spectroscopy. A broad absorption band spreading from approximately 3000 to 3600 cm^{-1} attributed to water molecules, together with the asymmetric stretching band (ν_3 mode, from approximately 1360 cm^{-1} to 1580 cm^{-1}) and the out-of-plane bending band (ν_2 mode, at around 870 cm^{-1}) of the carbonate ions are clearly visible for nanoparticles but not for micron particles. In contrast, the stretching band at 3570 cm^{-1} originating from OH^- ions is visible for micron but not for nanoparticles (Supplementary Fig. 4). Solid-state

One dimensional (1D) ^{1}H and ^{31}P single-pulse (SP) magic angle spinning (MAS) Nuclear Magnetic Resonance (NMR) was performed to provide further information on compositional and structural features. Spectra of the nano and micron particles differ greatly in their spectral widths (full width at half maximum, FWHM = 2.9 ± 0.1 ppm and 0.9 ± 0.1 ppm for nano and micron particles, respectively), with a broader distribution of chemical environments appearing in nano particles, supporting our earlier XRD analysis data (Supplementary Fig. 5). In addition, the ^{1}H SP MAS NMR spectrum of nanoparticles also display a broad and intense composite signal observable in the range of $\delta^{1}H$ = 5-17 ppm. This signal not only shows the presence of structural water molecules observable at $\delta^{1}H$ = 5.5 ppm, but also the presence of acidic phosphate species observable in the form of a downfield shoulder up to $\delta^{1}H$ = 17.0 ppm. These acidic phosphate species, that are also detected in bone hydroxyapatite *(22)*, were recently demonstrated to be HPO_4^{2-} ions based on accurate interatomic distance measurements *(23)*.

To further investigate the chemical environments of these hydrogen-bearing species, two-dimensional (2D) $\{^{1}H\}^{31}P$ Heteronuclear Correlation (HetCor) MAS NMR spectra of nano and micron HA particles were recorded (Fig. 1A iii & iv). These spectra are in the form of proton-phosphorus correlation maps in which the different signals, named “correlation peaks”, reveal the presence of atomic-scale spatial proximities among rigid hydrogen-bearing [displayed along the vertical (F1) dimension] and phosphorus-bearing species [displayed along the horizontal (F2) dimension]. On the one hand, the upper correlation peak observable at $\delta^{1}H$ = 0.0 ppm in the vertical (F1) dimension is present both particles and corresponds to OH^- ions near PO_4^{3-} ions in hydroxyapatite structure. On the other hand, a lower correlation peak observable in the range of $\delta^{1}H$ = 5-17 ppm in the vertical (F1) dimension is only present for the nanoparticles. The molar proportion of HPO_4^{2-} and PO_4^{3-} ions respectively present in the amorphous surface layer and in the

apatitic crystalline core were found to be approximately 40/60 for nanoparticles (Supplementary Fig. 6 & 7), whereas a value of 50/50 was determined for bone hydroxyapatite from a mature bone tissue sample *(23)*. It should be noted that differences in stoichiometry between the two particles formulations may be attributed to the fabrication process(es). Given the similarity of our in-house generated nanoparticles to bone hydroxyapatite, we refer to these particles as bone mimetic nanoparticles (BMnP).

Hydroxyapatite particle size influences pro-inflammatory cytokine expression by primary human macrophages.

We have previously demonstrated that micron-sized hydroxyapatite (HA) particles directly drive polarization of human macrophages towards a pro-inflammatory M1 phenotype *(24)*. The immune response to nano-sized hydroxyapatite particles has not yet been assessed in human immune cells therefore we compared the immune modulating properties of BMnP to commercially available micron-sized particles. We first tested both particles for any contaminating LPS and found that the concentration of endotoxin (LPS) was below the threshold level for TLR4 activation as determined using the HEK-Blue LPS detection kit (Supplementary Fig. 8). Primary human macrophages were stimulated with each particle type for 24 hours and cytokine/chemokine production was quantified by ELISA. Micron HA significantly enhanced production of the pro-inflammatory cytokine, TNFα, and the chemokine, IL-8, when compared with untreated controls, whereas BMnP treatment failed to induce production of either of these inflammatory mediators. In contrast, the anti-inflammatory cytokine, IL-10, was significantly upregulated by the BMnP. Of note, neither particle size induced production of the pleiotropic cytokine, IL-6 (Fig. 1B). We also demonstrate that micron, but not nanoparticles, significantly upregulate the production of IL-1β and its co-

secreted isoform, IL-1α, in LPS primed macrophages, suggesting that the smaller particles are below the size range required to activate the NLRP3 inflammasome (Fig. 1C). This is in contrast to findings in murine dendritic cells which demonstrated NLRP3-dependent IL-1β production by hydroxyapatite particles in the 100nm size range *(25)*. Finally, experiments were conducted to identify potential factors involved in nanoparticle induced IL-10 secretion. It has been reported that IL-10 expression is regulated by the transcription factor, cMaf, which is in turn upregulated by the signaling molecule STAT3 *(26, 27)*. Treatment of macrophages for 24 hours with micron HA or BMnP revealed that the latter is indeed capable of driving cMaf expression, and that BMnP also activates STAT3, as indicated by enhanced phosphorylation of STAT3 15-30 minutes post cell stimulation (Fig. 1D). Taken together these results suggest that nano-sized particles are significantly less inflammatory than micron-sized HA particles and are capable of driving the production of the anti-inflammatory cytokine IL-10, and this may occur in a STAT3/cMaf dependent manner.

Bone mimetic nanoparticles drive anti-inflammatory M2 macrophage polarization.

The impact of particle size on macrophage phenotype was next assessed by examining expression of established M1 and M2 macrophage-associated markers following particle treatment. Cells were also stimulated with, LPS and IFN-γ or IL-4 as a positive control for M1 and M2 macrophage activation respectively. Flow cytometric analysis revealed that, similar to LPS and IFNγ, micron particles significantly increased expression of the M1 surface marker, CD86. In contrast, nanoparticles (BMnP) did not induce M1-associated markers, but significantly enhanced surface expression of the M2-associated markers, CD163 and CD206, and the response seen was greater than that induced by IL-4 (Fig. 2A). Furthermore, micron particles promoted robust expression of

the M1-associated genes, CXCL11 and CCL19, as assessed by real-time PCR, whereas nanoparticles induced significant expression of the M2 associated genes *(28)*, MRC1 and CCL13 (Fig. 2B). This was confirmed at the protein level by immunoblotting for CD163 and CD206 (Fig. 2C) and immunofluorescent staining for CD206 and the M1 marker, CD80 (Fig. 2D). Recent research suggests that M1 and M2 macrophages exhibit differences in cell shape and morphology *(29)*, with M1 macrophages assuming a more elongate and irregular shape compared to M2 macrophages which are circular in appearance *(30)*. In agreement with this, we found that nanoparticle-treated macrophages exhibited a higher circularity index compared to macrophages treated with micron-particles, which appeared to have a decreased circularity index and a large perimeter value (Fig. 2E). Finally, we fluorescently tagged the MPs and BMnPs and assessed their uptake by macrophages using fluorescence microscopy. Both particle types are taken up within 1 hr of treatment, and while not significant, it would appear that the BMnPs are taken up at a higher level than MPs (Supplementary Fig. 9A & 9B). Furthermore, both particles are localised to the cytoplasmic space, with some clustering evident at the cell membrane. Pre-treatment of cells with Latrunculin B (a commonly used inhibitor of phagocytosis) significantly reduced microparticle-induced expression of M1 markers, while having no effect on nanoparticle-induced M2 marker expression (Supplementary Fig. 9C-F). While further study is required, we can suggest from this new data, that the larger particles are taken up by phagocytosis while the BMnPs may enter the cell via by pinocytosis or endocytosis. Indeed, this has previously been demonstrated for particles in the nanometre range *(31)*. Taken together, these results suggest that bone mimetic nanoparticles are potent drivers of M2-type polarized human macrophages.

Conditioned media from nanoparticle treated macrophages enhances MSC osteogenic differentiation and migration.

It is well established that macrophages play a significant role in tissue repair and regeneration, therefore, we next sought to determine whether the osteogenic differentiation capacity of MSCs is influenced by macrophage phenotype/secreted factors following exposure to hydroxyapatite particles. Human MSCs were cultured for 48 hours in particle free conditioned media (CM) from macrophages treated for 24 hours with micron or nano-sized HA particles. Real-time PCR analysis revealed that CM from nanoparticle treated macrophages significantly enhanced mRNA expression of the osteogenic genes, bone morphogenetic protein 2 (*bmp2)* and alkaline phosphatase (*alp*) in MSCs, when compared to CM from untreated macrophages or CM from micro particle treated macrophages (Fig. 3A). There was a non-significant trend towards increased OPN expression with CM from micro particle-treated macrophages, however, expression of OCN was not significantly affected by any treatment (Fig. 3A) nor was expression of the osteogenic transcription factors, Runx2 and Osterix, which work together to upregulate OPN (Supplementary Fig. 12A). Assessment of mineralisation and calcification by Alizarin Red staining after 7 days revealed an enhanced appearance of calcification granules in the nanoparticle-CM treated MSCs (Fig. 3B), which was verified following dye extraction and quantification (Fig. 3C). This suggests that BMnP CM, which consists primarily of an M2-like secretome, can enhance early matrix mineralisation of MSCs. Importantly, CM was shown to be free of any residual particles (Supplementary Fig. 1), and while there was a trend towards osteogenic gene expression upon treatment with the particles alone, this is not significant. Furthermore, we don't observe any difference between the MP and BMnP under these conditions. (Supplementary Fig. 10A). Furthermore, particles were incubated for 24h in cell-free media to control for any material release

and no discernible differences in MSC osteogenic gene expression was observed under these conditions (Supplementary Fig. 10B). Infiltration and recruitment of host MSCs into any tissue-engineered construct is an important factor for consideration given their role in ECM deposition, therefore, in addition to osteogenic differentiation, the migratory capacity of the MSCs was assessed using an *in vitro* scratch assay as a model of wound healing. (Fig. 3D). Semi-quantitative analysis of cell repopulation at the wound site within 24 hours revealed a significantly higher number of MSCs migrating back across the wound margin (Fig. 3E). Importantly there were no differences in the total cell number in each group, eliminating the possibility that the differences observed were due to cell proliferation (Fig. 3F). Taken together, these results suggest that secreted factors from nanoparticle polarized macrophages promote osteogenic differentiation of MSCs and enhance MSC migratory capacity.

BMnP drive pro-angiogenic responses in primary human macrophages and endothelial cells. As vascularization and angiogenesis are crucial processes in bone tissue repair *(32)*, we next assessed the capacity of micron and nano particles to drive angiogenic responses in primary human macrophages and the HUVEC endothelial cell line. Primary human macrophages were stimulated with micron and nano particles for 24 hours and mRNA expression of the angiogenic genes, VEGF and Ang1, were assessed using real-time PCR. While both micron and nanoparticles significantly increased mRNA expression of VEGF, increased expression levels of Ang1 were only observed in nano particle treated cells (Fig. 4A). Furthermore, conditioned media from nano particle treated macrophages significantly enhanced tube formation in HUVECs as evidenced by increased branching, branch length and junction formation between cells which was comparable to treatment with the positive control, VEGF (Fig. 4B & 4C).

Conditioned media from nanoparticle treated macrophages drives osteogenesis and mineralization of human MSCs in an IL-10 dependent manner.

The role of various cytokines in osteogenesis has gained much attention, in particular TNFα and IL-1β *(33–35)*. Given our demonstration that nanoparticles can drive robust IL-10 expression, we sought to determine if this cytokine plays a role in nanoparticle-driven MSC differentiation. Macrophages were pre-treated with anti-IL-10 neutralizing antibody or an isotype control antibody prior to treatment with micron or nanoparticles for 24 hours. MSC were then cultured for 48 hours in CM from treated macrophages. Consistent with the observations above, CM from nanoparticle treated macrophages enhanced BMP2 and ALP mRNA expression, however expression of both genes was significantly reduced when MSC were cultured in CM from particle-treated macrophages that were pre-incubated with anti-IL-10 (Fig. 5A). While OPN expression was enhanced in MSC cultured in CM from micron particle-treated macrophages, IL-10 neutralization had no effect on gene expression (Fig. 5A), suggesting that the pro-osteogenic effects of nanoparticles may be largely attributed to IL-10. Furthermore, the same effects were observed when IL-10 was neutralized in the MSC culture (Supplementary Fig. 11 A & B). This was further supported by the apparent lack of downstream mineralization and calcification of MSCs after 7 days when IL-10 was neutralized (Fig. 5B & C). No differences were observed in cells treated with the IgG isotype control antibody, confirming the role of IL-10 (Supplementary Fig. 12B). Furthermore, pre-treatment of macrophages with the IL-10 neutralizing antibody did not affect BMnP-induced M2 macrophage polarization, based on expression of the M2 markers, MRC1 and CCL13. This was also the case with the positive control, IL-4, suggesting that the effects observed are more likely mediated by IL-10 signaling in the MSCs rather than IL-10 induced macrophage polarization (Supplementary Fig. 11 C-D). Finally, direct addition of recombinant human (Rh) IL-

10 to MSCs resulted in a significant induction of ALP, OPN and BMP2 but not OCN (Fig. 4D) after 48 hours, while supplementation of culture media with Rh IL-10 resulted in significantly more calcification and mineralization of MSCs after 7 days (Fig. 5E & 5F), providing further evidence for a direct role for IL-10 in early osteogenesis and mineralization.

Characterization of immune cell subsets and phenotype following implantation of hydroxyapatite functionalized scaffolds into a rat femoral defect model.

In order to translate the *in vitro* data to a physiologically relevant *in vivo* system, we characterized the immune response to hydroxyapatite functionalized ECM scaffolds using a rat femoral defect model *(19)*. Scaffolds were prepared from porcine articular cartilage (AC) and growth plate (GP) and assessed for inherent immunogenicity by co-culturing with primary human macrophages. Macrophage cytokine production was negligible in response to AC ECM derived scaffolds, whereas significant TNFα, IL-6 and IL-8 production was observed upon culture of macrophages with GP ECM derived scaffolds (data not shown). AC derived scaffolds were therefore functionalized with micron or nano-sized HA particles for use in the *in vivo* defect model (Fig. 5a). SEM imaging and pore size analysis confirmed that the functionalized scaffolds had an average pore size of 50 μm (Supplementary Fig. 13A & B) which is in the range suitable for cell infiltration *(36, 37)*. Moreover, the calculated porosity of both scaffold types was in the range of 95-97% (Supplementary Fig 13C). Electron dispersive X-ray (EDX) microscopy demonstrated that scaffolds were effectively functionalized after processing (containing both calcium and phosphate) (Fig. 6A). Importantly, incorporation of particles into the scaffolds did not affect their ability to differentially polarize macrophages *in vitro*, as evidenced by induction of the M1 macrophage marker, CXCL11, by micron HA functionalized scaffolds and the M2 macrophage

marker, MRC1, by BMnP functionalized scaffolds (Supplementary Fig. 13 E & F). Functionalized scaffolds were implanted into a 5 mm femoral defect and repair tissue was harvested for analysis 1 week post-implantation (Fig. 6B). Flow cytometric analysis of immune cell subsets at the defect site revealed no discernible difference in the number of B cells ($CD45^+$ $CD19^+$ Siglec F^-), but showed significant infiltration of T cells ($CD45^+CD3^+CD19^-$) and neutrophils ($CD45^+CD11b^+Ly6G^+$), indicative of a more pro-inflammatory microenvironment in tissue samples from rats implanted with micron HA functionalized scaffolds but not BMnP functionalized scaffolds. While there was a trend towards enhanced numbers of macrophages in rats implanted with HA functionalised scaffolds, this was not significant (Fig. 6C). There was no significant difference in immune cell infiltration in samples taken outside the defect area (Supplementary Fig. 14). Individual T cell subsets were not assessed as part of this study, however, serum cytokine analysis revealed higher concentrations of the Th1-associated cytokine, IFNy, in the micron HA-treated rats. Conversely, circulating concentrations of the anti-inflammatory cytokine, IL-10, were higher in the BMnP group versus the empty defect ($p=0.065$) and significantly higher than the MP-treated rats (Fig. 6D). Analysis of surface marker expression on macrophages ($CD11b^+$ $F4/80^+$) revealed no change in the absolute numbers of macrophages positive for CCR2, CD86 or CX3CR1, (Supplementary Fig 15). However macrophages obtained from rats that had been implanted with micron HA functionalized scaffolds upregulated surface marker expression of CCR2 and CD86, whereas cells from rats implanted with BMnP-functionalized scaffolds expressed higher levels of CX3CR1 (Fig. 6E). Overall, these results indicate that larger micron particles are primarily driving a pro-inflammatory host response, while nanoparticles promote an anti-inflammatory immune profile.

BMnP functionalized scaffolds accelerate bone formation following implantation into a rat femoral defect model.

Given the link between inflammation and bone regeneration, defect repair and new bone formation was analyzed at 1 and 4 weeks post implantation. Hematoxylin and Eosin (H & E) staining of the defect site at 1 week demonstrated poor cell infiltration in rats implanted with micron HA functionalized scaffolds, while both empty defect and BMnP functionalized scaffold groups showed homogenous infiltration of cells into the scaffold and defect site (Fig. 7A). Furthermore, we observed a thick fibrous layer consisting of multinucleated cells surrounding the implant in the micron HA scaffold group (Fig. 7A (i) and (ii)). This is indicative of fibrous encapsulation which can often occur after construct implantation and prevents infiltrating cells from gaining access to the center of the defect, ultimately resulting in less extracellular matrix being deposited *(38)*. Vascularization is also an essential aspect of functional bone tissue regeneration *(39)*, therefore, we next examined the capacity of these scaffolds to induce vessel formation. BMnP functionalized scaffolds, but not micron HA functionalized scaffolds, promoted the formation of vessel-like structures (Fig. 7A, lower panel), that stained positively for vWF and α-SMA, indicating the presence of vascular endothelial cells (Fig. 7B). This is consistent with previous studies demonstrating that prolonged administration of inflammatory cytokines impairs angiogenesis *(39, 40)*, while an anti-inflammatory environment can promote angiogenesis and vascularization *(41, 42)*. The presence of vessels in tissue-engineered constructs is particularly important as efficient vascularization in large bone defects still remains a key challenge. Therefore, we next used μCT analysis to assess and quantify new bone formation in the defect site and to determine whether the early differences in inflammatory profile and vessel formation would result in differences in downstream bone formation. At 4 weeks post implantation, the total bone volume in the BMnP

functionalized scaffold group was significantly increased compared to micron HA functionalized scaffolds, which failed to bridge or have any mineral matrix deposition in the defect site (Fig. 7C & 7D). Furthermore, quantitative densitometric analysis revealed a lower bone density (mg HA/cm^3) in the micron HA functionalized scaffold group (Fig. 7E). Taken together, this suggests that BMnP functionalized scaffolds are capable of driving mineral matrix deposition in addition to promoting the formation of vessels at the defect site and are therefore superior to micron HA functionalized scaffolds in the bone regeneration process.

Discussion

There is now substantial evidence indicating that immune cells interact with the skeletal system and play a temporal role in post injury healing responses *(33, 34, 43)*. Inflammation peaks at 24 hours post bone injury and is characterized by the expression of pro-inflammatory cytokines and factors that contribute to early angiogenesis. This is followed by a renewal phase, 7-10 days after injury, where bone forms via intramembranous ossification *(43–45)*. Pro-inflammatory mediators are absent during the renewal phase, which is driven by factors influencing endochondral bone formation, such as TGF-β1-3 and bone morphogenetic proteins *(43, 46)*. An imbalance in immune-mediated responses during early fracture healing is hypothesized to disturb the regeneration cascade leading to suboptimal bone healing, hence, the incorporation of bioactive cues into ECM scaffolds that are capable of polarizing immune responses has been hailed as a potential strategy to enhance constructive bone remodeling. In this study, we demonstrate that our micron HA particles appear as a more stoichiometric hydroxyapatite with a formula close to $Ca_{10}(PO_4)_6(OH)_2$ *(22)*. This is in contrast to our in-house generated nano-sized hydroxyapatite particles, which are very similar to that of natural bone hydroxyapatite, with a crystalline core in the form of

hydroxyapatite, coated by a mineral amorphous surface layer *(47–49)*. We demonstrate that these bone mimetic nanoparticles (BMnPs) preferentially polarize human macrophages towards an M2 phenotype and specifically enhance production of the anti-inflammatory cytokine, IL-10. Furthermore, the secretome from BMnP treated macrophages enhances MSC osteogenesis in an IL-10 dependent manner, demonstrating a direct pro-osteogenic role for this cytokine. Further studies are required to determine if contact dependent mechanisms are also capable of influencing macrophage-induced MSC osteogenesis. Higher numbers of CX3CR1 expressing M2 macrophages were observed in a femoral defect model when rats were implanted with BMnP functionalized ECM scaffolds. In contrast, tissue samples obtained from rats implanted with MP functionalized scaffolds exhibited higher numbers of T cells, neutrophils and M1 macrophages, all indicative of a more pro-inflammatory microenvironment. Furthermore, bone volume was significantly enhanced in the rats treated with BMnP compared with rats implanted with MP functionalized scaffolds, indicating that this material has inherent immune modulating as well as pro-regenerative properties.

IL-10 has previously been reported to promote chondrogenic differentiation and chondrocyte proliferation via the BMP pathway. The same study also demonstrated that IL-10 deficient mice exhibit a reduction in the proliferation zone of embryonic growth plates *(50)*. We found that the secretome of BMnP-treated macrophages enhanced expression of the osteogenic genes, BMP2 and ALP in human MSCs, while blockade of IL-10 reduced subsequent calcification and mineralization, further supporting a role for IL-10 in BMP2 mediated osteogenic differentiation. Increased expression of BMP2, ALP and OPN was also observed in the presence of recombinant IL-10, and while IL-10 was capable of driving OPN expression in MSCs, the same was not observed for BMnPs. An in-depth proteomic analysis is required to provide further

information regarding the composition of the BMnP-macrophage secretome as there are likely a number of factors, in addition to IL-10, that are contributing to the observed outputs.

Higher concentrations of circulating IL-10 were observed in rats implanted with BMnP functionalized scaffolds and, while the specific source of IL-10 was not identified in this study, we did observe higher numbers of cells expressing CX3CR1 a marker of M2 macrophages *(51, 52)*. The heightened anti-inflammatory phenotype was accompanied by elevated levels of vWF and α-SMA expressing vessels and vascularization in rats implanted with BMnP functionalized scaffolds compared to MP functionalized scaffolds. Of note, $CX3CR1^{+}$ cells have been shown to play an important role in neovascularization and the promotion of angiogenesis in a model of hind-limb ischemia *(53)*, suggesting that the BMnP-induced $CX3CR1^{+}$ cell subset may be directly influencing vascularization in our femoral defect model. In support of this, treatment of macrophages with BMnP upregulated the expression of Ang1 (Fig. 4A), which is known to contribute to blood vessel maturation and stability *(54)*. Furthermore, conditioned media from BMnP-treated macrophages significantly enhanced angiogenic processes in the HUVEC endothelial cell line. While further in vivo study is required to assess blood vessel formation and vascularization, this data further supports the pro-angiogenic potential of the BMnP particles.

Given the inflammatory profile of the micron HA functionalized scaffolds and the apparent lack of tissue vascularization, which is a crucial component of functional bone regeneration *(39)*, it was not surprising that these early responses coincided with a lack of bone regeneration. Defect bridging was absent 4 weeks post implantation and there appeared be an appreciable decrease in bone density. In contrast, implantation of BMnP functionalized ECM scaffolds into critically sized bone defects resulted in significantly more new bone deposition compared to micron HA functionalized scaffolds. While full defect bridging was also absent in the BMnP scaffold group

at the 4 week time-point, future studies will explore combining M2-polarizing BMnP functionalized scaffolds with skeletal stem cells and/or osteogenic growth factors to determine if this will synergistically enhance long-term matrix deposition, tissue repair and functional bone regeneration. Current strategies being explored include incorporating anti-inflammatory cytokines such as IL-10 or IL-4 into bioscaffolds *(13–15)*. However, the data present here offers compelling evidence that nanoHA particles themselves are inherently anti-inflammatory and supportive of osteogenesis.

Conclusions

In summary, our data positions nano-sized HA particles as a particularly attractive immune-modulatory biomaterial that may be incorporated into various 3D constructs, and while future studies are required to fully elucidate the role of IL-10 in nanoparticle-mediated responses, the use of these bioactive particles may either avoid the need to exogenously load cytokines into ECM constructs or indeed complement their use.

Data availability

The authors declare that all data supporting the finding of this study are available within the paper and its Supplementary Information

Acknowledgments:

Funding: OM is supported by Trinity College Dublin, Postgraduate Research Scholarship; AD is supported by the Health Research Board, Ireland (ILP/POR/2017/041); IW is supported by European Regional Development Fund (Grant Number 13/RC/2073). DK is supported by Science Foundation Ireland (12/IA/1554; 12/US/12489), European Research Council (ERC-2014CoG-

647004). KC is supported by the Irish Research Council and KHGM is supported by Science Foundation Ireland (grant 16/IA/4468); SVE was supported by the European Union's Horizon 2020 research and innovation program under the Marie Sklodowska-Curie grant agreement No 793861.

Author contributions: A.D, O.R.M, D.J.K. conceived the study, designed experiments, interpreted results and wrote the manuscript. O.R.M conducted experiments with laboratory assistance and intellectual input from T.G.F, I.T.W, D.C.B, S.V.E, K.C, V.N, K.H.G.M and P.P and surgical assistance from D.C.B and P.P. S.V.E and C.H. performed particle characterisation experiments. All authors have given approval to the final version of the manuscript.

Competing interests: The authors declare no conflicts of interest.

References

1. G. C. Reilly, A. J. Engler, Intrinsic extracellular matrix properties regulate stem cell differentiation, *J. Biomech.* **43**, 55–62 (2010).

2. C. M. Murphy, A. Matsiko, M. G. Haugh, J. P. Gleeson, F. J. O'Brien, Mesenchymal stem cell fate is regulated by the composition and mechanical properties of collagen–glycosaminoglycan scaffolds, *J. Mech. Behav. Biomed. Mater.* **11**, 53–62 (2012).

3. J.-H. Lee, H.-K. Park, K. S. Kim, Intrinsic and extrinsic mechanical properties related to the differentiation of mesenchymal stem cells, *Biochem. Biophys. Res. Commun.* **473**, 752–757 (2016).

4. K. Sadtler, K. Estrellas, B. W. Allen, M. T. Wolf, H. Fan, A. J. Tam, C. H. Patel, B. S. Luber, H. Wang, K. R. Wagner, J. D. Powell, F. Housseau, D. M. Pardoll, J. H. Elisseeff, Developing a pro-regenerative biomaterial scaffold microenvironment requires T helper 2 cells., *Science* **352**, 366–370 (2016).

5. N. Grotenhuis, S. F. H. De Witte, G. J. V. M. van Osch, Y. Bayon, J. F. Lange, Y. M. Bastiaansen-Jenniskens, Biomaterials Influence Macrophage–Mesenchymal Stem Cell Interaction *In Vitro*, *Tissue Eng. Part A* **22**, 1098–1107 (2016).

6. Z. Julier, A. J. Park, P. S. Briquez, M. M. Martino, Promoting tissue regeneration by modulating the immune system, *Acta Biomater.* **53**, 13–28 (2017).

7. G. E. Glass, J. K. Chan, A. Freidin, M. Feldmann, N. J. Horwood, J. Nanchahal, TNF- promotes fracture repair by augmenting the recruitment and differentiation of muscle-derived stromal cells, *Proc. Natl. Acad. Sci.* **108**, 1585–1590 (2011).

8. J. Hashimoto, H. Yoshikawa, K. Takaoka, N. Shimizu, K. Masuhara, T. Tsuda, S. Miyamoto, K. Ono, Inhibitory effects of tumor necrosis factor alpha on fracture healing in rats, *Bone* **10**, 453–457 (1989).

9. C. Schlundt, T. El Khassawna, A. Serra, A. Dienelt, S. Wendler, H. Schell, N. van Rooijen, A. Radbruch, R. Lucius, S. Hartmann, G. N. Duda, K. Schmidt-Bleek, Macrophages in bone fracture healing: Their essential role in endochondral ossification., *Bone* (2015), doi:10.1016/j.bone.2015.10.019.

10. D. Toben, I. Schroeder, T. El Khassawna, M. Mehta, J.-E. Hoffmann, J.-T. Frisch, H. Schell, J. Lienau, A. Serra, A. Radbruch, G. N. Duda, Fracture healing is accelerated in the absence of the adaptive immune system., *J. Bone Miner. Res.* **26**, 113–124 (2011).

11. J. Michel, M. Penna, J. Kochen, H. Cheung, Recent Advances in Hydroxyapatite Scaffolds Containing Mesenchymal Stem Cells, *Stem Cells Int.* **2015**, 1–13 (2015).

12. O. R. Mahon, S. O'Hanlon, C. C. Cunningham, G. M. McCarthy, C. Hobbs, V. Nicolosi, D. J. Kelly, A. Dunne, Orthopaedic implant materials drive M1 macrophage polarization in a spleen tyrosine kinase- and mitogen-activated protein kinase-dependent manner, *Acta Biomater.* **65** (2018), doi:10.1016/j.actbio.2017.10.041.

13. K. A. Glass, J. M. Link, J. M. Brunger, F. T. Moutos, C. A. Gersbach, F. Guilak, Tissue-engineered cartilage with inducible and tunable immunomodulatory properties., *Biomaterials* **35**, 5921–5931 (2014).

14. C. M. Dumont, J. Park, L. D. Shea, Controlled release strategies for modulating immune responses to promote tissue regeneration., *J. Control. Release* **219**, 155–166 (2015).

15. C. Holladay, K. Power, M. Sefton, T. O'Brien, W. M. Gallagher, A. Pandit, Functionalized scaffold-mediated interleukin 10 gene delivery significantly improves survival rates of stem cells in vivo., *Mol. Ther.* **19**, 969–978 (2011).

16. G. M. Cunniffe, F. J. O'Brien, S. Partap, T. J. Levingstone, K. T. Stanton, G. R. Dickson, The synthesis and characterization of nanophase hydroxyapatite using a novel dispersant-aided precipitation method., *J. Biomed. Mater. Res. A* **95**, 1142–1149 (2010).

17. V. Karageorgiou, D. Kaplan, Porosity of 3D biomaterial scaffolds and osteogenesis, *Biomaterials* **26**, 5474–5491 (2005).

18. D. C. Browe, A. Dunne, C. T. Buckley, D. J. Kelly, Glyoxal cross-linking of solubilised extracellular matrix to produce highly porous , elastic and chondro-permissive scaffolds for orthopaedic tissue engineering, , doi:10.1002/jbm.a.36731.

19. A. C. Daly, P. Pitacco, J. Nulty, G. M. Cunniffe, D. J. Kelly, 3D printed microchannel networks to direct vascularisation during endochondral bone repair, *Biomaterials* **162**, 34–46 (2018).

20. G. M. Cunniffe, G. R. Dickson, S. Partap, K. T. Stanton, F. J. O'Brien, Development and characterisation of a collagen nano-hydroxyapatite composite scaffold for bone tissue engineering., *J. Mater. Sci. Mater. Med.* **21**, 2293–2298 (2010).

21. T. Gonzalez-Fernandez, B. N. Sathy, C. Hobbs, G. M. Cunniffe, H. O. McCarthy, N. J. Dunne, V. Nicolosi, F. J. O'Brien, D. J. Kelly, Mesenchymal stem cell fate following non-viral gene transfection strongly depends on the choice of delivery vector., *Acta Biomater.* **55**, 226–238 (2017).

22. Y. Wang, S. Von Euw, F. M. Fernandes, S. Cassaignon, M. Selmane, G. Laurent, G. Pehau-Arnaudet, C. Coelho, L. Bonhomme-Coury, M.-M. Giraud-Guille, F. Babonneau, T. Azaïs, N. Nassif, Water-mediated structuring of bone apatite, *Nat. Mater.* **12**, 1144–1153 (2013).

23. S. Von Euw, Y. Wang, G. Laurent, C. Drouet, F. Babonneau, N. Nassif, T. Azaïs, Bone mineral: new insights into its chemical composition, *Sci. Rep.* **9**, 8456 (2019).

24. O. R. Mahon, S. O'Hanlon, C. C. Cunningham, G. M. McCarthy, C. Hobbs, V. Nicolosi, D. J. Kelly, A. Dunne, Orthopaedic implant materials drive M1 macrophage polarization in a spleen tyrosine kinase- and mitogen-activated protein kinase-dependent manner., *Acta Biomater.* **65**, 426–435 (2018).

25. F. Lebre, R. Sridharan, M. J. Sawkins, D. J. Kelly, F. J. O'Brien, E. C. Lavelle, The shape and size of hydroxyapatite particles dictate inflammatory responses following implantation., *Sci. Rep.* **7**, 2922 (2017).

26. J. Xu, Y. Yang, G. Qiu, G. Lai, Z. Wu, D. E. Levy, Y. Ding, c-Maf Regulates IL-10 Expression during Th17 polarization, *Journal* **48**, 5437–5447 (2009).

27. S. Cao, J. Liu, L. Song, X. Ma, The Protooncogene c-Maf Is an Essential Transcription Factor for IL-10 Gene Expression in Macrophages, *J. Immunol.* **174**, 3484–3492 (2005).

28. P. J. Murray, J. E. Allen, S. K. Biswas, E. A. Fisher, D. W. Gilroy, S. Goerdt, S. Gordon, J. A. Hamilton, L. B. Ivashkiv, T. Lawrence, M. Locati, A. Mantovani, F. O. Martinez, J.-L. Mege, D. M. Mosser, G. Natoli, J. P. Saeij, J. L. Schultze, K. A. Shirey, A. Sica, J. Suttles, I. Udalova, J. A. van Ginderachter, S. N. Vogel, T. A. Wynn, Macrophage Activation and Polarization: Nomenclature and Experimental Guidelines, *Immunity* **41**, 14–20 (2014).

29. H. M. Rostam, P. M. Reynolds, M. R. Alexander, N. Gadegaard, A. M. Ghaemmaghami, Image based Machine Learning for identification of macrophage subsets, *Sci. Rep.* **7**, 1–11 (2017).

30. M. Shayan, J. Padmanabhan, A. H. Morris, B. Cheung, R. Smith, J. Schroers, T. R. Kyriakides, Nanopatterned bulk metallic glass-based biomaterials modulate macrophage polarization, *Acta Biomater.* **75**, 427–438 (2018).

31. P. Foroozandeh, A. A. Aziz, Insight into Cellular Uptake and Intracellular Trafficking of Nanoparticles, *Nanoscale Res. Lett.* **13** (2018), doi:10.1186/s11671-018-2728-6.

32. J. Filipowska, K. A. Tomaszewski, Ł. Niedźwiedzki, J. A. Walocha, T. Niedźwiedzki, The role of vasculature in bone development, regeneration and proper systemic functioning, *Angiogenesis* **20**, 291–302 (2017).

33. D. C. Lacey, P. J. Simmons, S. E. Graves, J. A. Hamilton, Proinflammatory cytokines inhibit osteogenic differentiation from stem cells: implications for bone repair during inflammation., *Osteoarthr. Cartil.* **17**, 735–742 (2009).

34. M. M. Martino, K. Maruyama, G. A. Kuhn, T. Satoh, O. Takeuchi, R. Muller, S. Akira, Inhibition of IL-1R1/MyD88 signalling promotes mesenchymal stem cell-driven tissue regeneration., *Nat. Commun.* **7**, 11051 (2016).

35. K. Hess, A. Ushmorov, J. Fiedler, R. E. Brenner, T. Wirth, TNFalpha promotes osteogenic differentiation of human mesenchymal stem cells by triggering the NF-kappaB signaling pathway., *Bone* **45**, 367–376 (2009).

36. G. M. Cunniffe, P. J. Diaz-Payno, J. S. Ramey, O. R. Mahon, A. Dunne, E. M. Thompson, F.

J. O'Brien, D. J. Kelly, Growth plate extracellular matrix-derived scaffolds for large bone defect healing., *Eur. Cell. Mater.* **33**, 130–142 (2017).

37. G. M. Cunniffe, P. J. Díaz-Payno, E. J. Sheehy, S. E. Critchley, H. V. Almeida, P. Pitacco, S. F. Carroll, O. R. Mahon, A. Dunne, T. J. Levingstone, C. J. Moran, R. T. Brady, F. J. O'Brien, P. A. J. Brama, D. J. Kelly, Tissue-specific extracellular matrix scaffolds for the regeneration of spatially complex musculoskeletal tissues, *Biomaterials* **188**, 63–73 (2018).

38. R. Sridharan, A. R. Cameron, D. J. Kelly, C. J. Kearney, F. J. O'Brien, Biomaterial based modulation of macrophage polarization: a review and suggested design principles, *Mater. Today* **18**, 313–325 (2015).

39. K. L. Spiller, S. Nassiri, C. E. Witherel, R. R. Anfang, J. Ng, K. R. Nakazawa, T. Yu, G. Vunjak-Novakovic, Sequential delivery of immunomodulatory cytokines to facilitate the M1-to-M2 transition of macrophages and enhance vascularization of bone scaffolds., *Biomaterials* **37**, 194–207 (2015).

40. K. Schmidt-Bleek, H. Schell, N. Schulz, P. Hoff, C. Perka, F. Buttgereit, H. D. Volk, J. Lienau, G. N. Duda, Inflammatory phase of bone healing initiates the regenerative healing cascade, *Cell Tissue Res.* **347**, 567–573 (2012).

41. K. L. Spiller, R. R. Anfang, K. J. Spiller, J. Ng, K. R. Nakazawa, J. W. Daulton, G. Vunjak-Novakovic, The role of macrophage phenotype in vascularization of tissue engineering scaffolds, *Biomaterials* **35**, 4477–4488 (2014).

42. N. Jetten, S. Verbruggen, M. J. Gijbels, M. J. Post, M. P. J. De Winther, M. M. P. C. Donners, Anti-inflammatory M2, but not pro-inflammatory M1 macrophages promote angiogenesis in vivo, *Angiogenesis* **17**, 109–118 (2014).

43. L. C. Gerstenfeld, D. M. Cullinane, G. L. Barnes, D. T. Graves, T. A. Einhorn, Fracture healing as a post-natal developmental process: molecular, spatial, and temporal aspects of its regulation., *J. Cell. Biochem.* **88**, 873–884 (2003).

44. T. Kon, T. J. Cho, T. Aizawa, M. Yamazaki, N. Nooh, D. Graves, L. C. Gerstenfeld, T. A. Einhorn, Expression of osteoprotegerin, receptor activator of NF-kappaB ligand (osteoprotegerin ligand) and related proinflammatory cytokines during fracture healing., *J. Bone Miner. Res.* **16**, 1004–1014 (2001).

45. R. Dimitriou, E. Tsiridis, P. V. Giannoudis, Current concepts of molecular aspects of bone healing, *Injury* **36**, 1392–1404 (2005).

46. N.-C. Cheng, B. T. Estes, H. A. Awad, F. Guilak, Chondrogenic differentiation of adipose-derived adult stem cells by a porous scaffold derived from native articular cartilage extracellular matrix., *Tissue Eng. Part A* **15**, 231–241 (2009).

47. M. J. Glimcher, Bone: Nature of the Calcium Phosphate Crystals and Cellular, Structural, and Physical Chemical Mechanisms in Their Formation, *Rev. Mineral. Geochemistry* **64**, 223–282 (2006).

48. S. Von Euw, W. Ajili, T.-H.-C. Chan-Chang, A. Delices, G. Laurent, F. Babonneau, N. Nassif, T. Azaïs, Amorphous surface layer versus transient amorphous precursor phase in bone – A case study investigated by solid-state NMR spectroscopy, *Acta Biomater.* **59**, 351–360 (2017).

49. C. Rey, C. Combes, C. Drouet, H. Sfihi, A. Barroug, Physico-chemical properties of nanocrystalline apatites: Implications for biominerals and biomaterials, *Mater. Sci. Eng. C* **27**, 198–205 (2007).

50. Y.-K. Jung, G.-W. Kim, H.-R. Park, E.-J. Lee, J.-Y. Choi, F. Beier, S.-W. Han, Role of interleukin-10 in endochondral bone formation in mice: anabolic effect via the bone morphogenetic protein/Smad pathway., *Arthritis Rheum.* **65**, 3153–3164 (2013).

51. L. Landsman, L. Bar-on, A. Zernecke, K. Kim, R. Krauthgamer, S. A. Lira, I. L. Weissman, C. Weber, S. Jung, W. Dc, E. Shagdarsuren, CX3CR1 is required for monocyte homeostasis and atherogenesis by promoting cell survival, *Blood* **113**, 963–972 (2009).

52. F. Geissmann, S. Jung, D. R. Littman, Blood Monocytes Consist of Two Principal Subsets with Distinct Migratory Properties Frederic, *Immunity* **129**, 470–485 (2018).

53. Y. Park, J. Lee, J.-Y. Kwak, K. Noh, E. Yim, H.-K. Kim, Y. J. Kim, H. E. Broxmeyer, J.-A. Kim, Fractalkine induces angiogenic potential in CX3CR1-expressing monocytes, *J. Leukoc. Biol.* , jlb.1A0117-002RR (2017).

54. E. Conway, D. Collen, P. Carmeliet, Molecular mechanisms of blood vessel formation., *Trends Biochem. Sci.* **22**, 251–256 (2001).

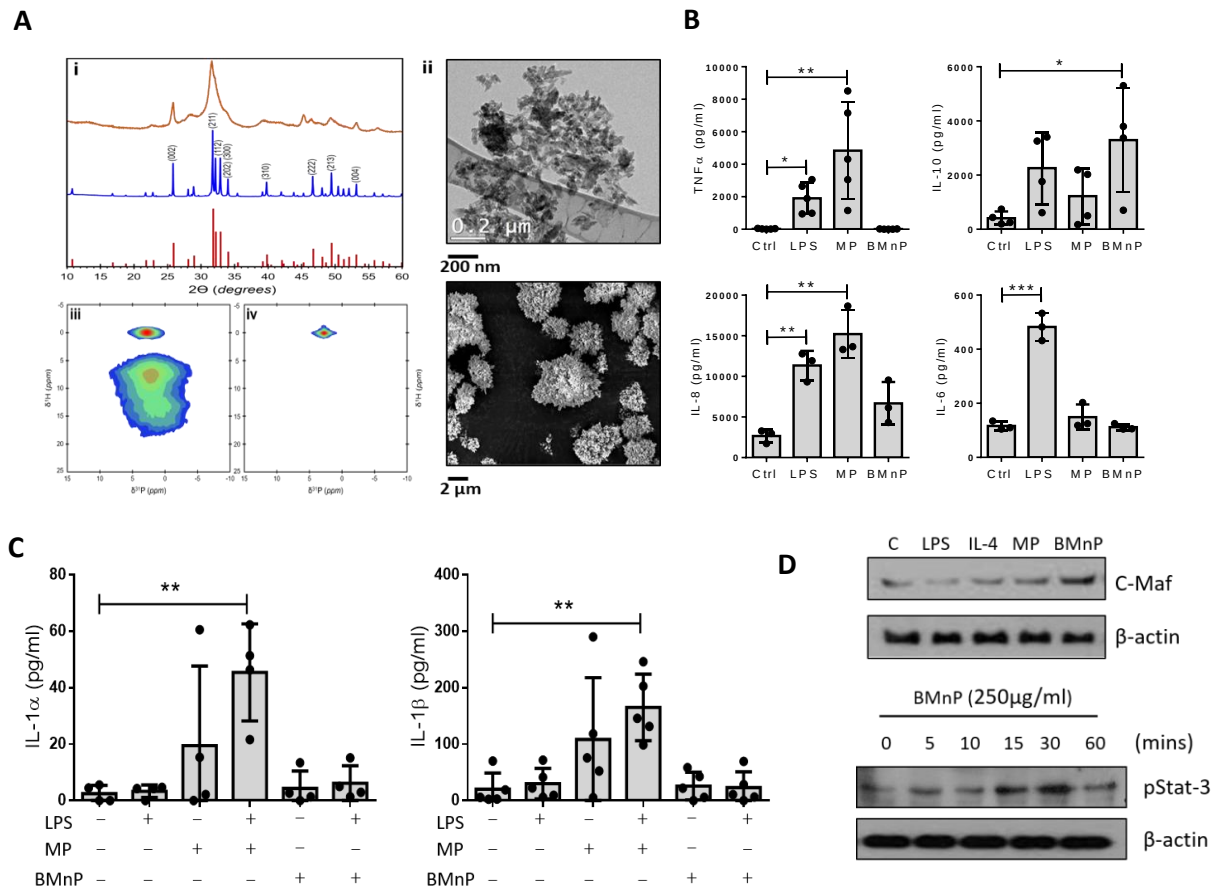

Fig. 1. Micron and nano Hydroxyapatite particles drive differential cytokine production by primary human macrophages. (A) (i) Powder X-ray diffraction (XRD) patterns of nano (orange line) and micron (blue line) hydroxyapatite particles, together with the theoretical XRD pattern of hydroxyapatite (red lines, JCPDS file No. 9-432). (**ii**) A representative transmission electron micrograph (TEM) of the nanoparticles; and a representative scanning electron micrograph (SEM) of the micron particles. (**iii and iv**) Two-dimensional (2D) $\{^{1}H\}^{31}P$ Heteronuclear Correlation (HetCor) NMR spectra of nanoparticles (C) and micron particles (D). **(B)** Primary human macrophages (1x 10^{6} cells/ml) were stimulated with particles (250 µg/ml) for 24 hours. Cell supernatants were assessed for TNFα, IL-10, IL-8 and IL-6 by ELISA. **(C)** Primary human macrophages (1x 10^{6} cells/ml) were primed with LPS (100 ng/ml) for 2 hours prior to treatment

with particles (250 µg/ml) for 24 hours. IL-1α and IL-1β cytokine production was quantified in cell supernatants by ELISA. **(D)** Primary human macrophages (1x 10^6 cells/ml) were treated with LPS (100 ng/ml), IL-4 (20 ng/ml) or particles (250 µg/ml) for 24 hours, and upregulation of c-Maf protein was detected by immunoblotting. Alternatively, cells were stimulated with nanoparticles (250 µg/ml) over the course of 60 minutes and Stat-3 activation as indicated by phosphorylation was detected by immunoblotting using phospho-specific antibodies. Results shown are means (+/- SEM) for triplicate cultures of 3-5 independent human donors. Statistical differences were assessed using Kruskal Wallis test with Dunn's post-test, *$p<0.05$, **$p<0.01$, ***$p<0.001$. (MP=micron sized HA; BMnP=bone mimetic nano particles)

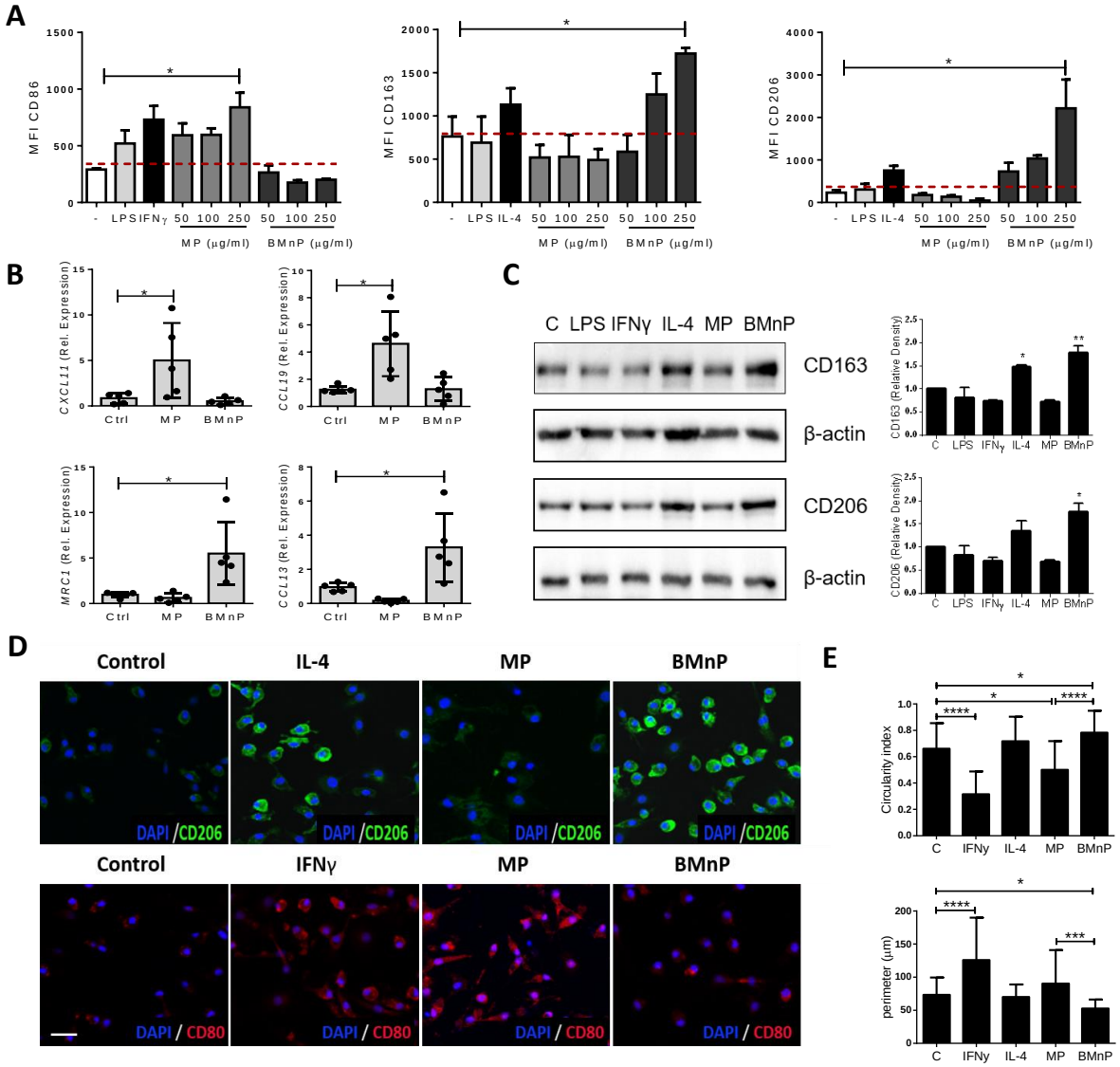

Fig. 2. nanoparticles polarize M2-type macrophages. (A) Primary human macrophages (1x 10^6 cells/ml) were treated with micron particles or nanoparticles (50, 100 or 250 µg/ml) for 6 hours prior to staining with fluorochrome-conjugated antibodies against CD86, CD163 or CD206 and analyzed by flow cytometry. Results shown are means (+/-SEM) for 3 independent experiments. Statistical differences were assessed using Kruskal Wallis test with Dunn's post-test, *p<0.05 vs untreated control. **(B)** Primary human macrophages (1x 10^6 cells/ml) were stimulated particles (250 µg/ml) for 24 hours. mRNA levels of CXCL11, CCL19, MRC1 and CCL13 were analyzed

by qRT-PCR. Results shown are means (+/- SEM) for triplicate cultures of 5 independent donors. Statistical differences were assessed using one-way ANOVA with Tukey post-test. *p<0.05. **(C)** Primary human macrophages (1x 10^6 cells/ml) were treated with LPS (100 ng/ml), IFNγ (20 ng/ml), IL-4 (20 ng/ml) or particles (250 µg/ml) for 24 hours. Upregulation of CD206 and CD163 protein was detected by immunoblotting using antibodies specific for CD206 and CD163. Densitometric analysis of 2 immunoblots was performed using image J software. Bar graphs illustrate the mean (+/-SD) increase in protein expression of CD206 or CD163 relative to untreated sample (C) and normalized to β-actin protein. Statistical differences were assessed using a one-way ANOVA with Tukey post-test, *p<0.05, **p<0.01. **(D)** Immunofluorescence staining images of primary human macrophages (0.5 x 10^6 cells/ml) treated with particles (250 µg/ml) for 24 hours or the positive controls IL-4 (20 ng/ml) or IFNγ (20 ng/ml). CD206 (green) and CD80 (red), DAPI in blue. Magnification =20x. Scale bar = 50µm. **(F)** Cell shape parameter analysis using image J software. Statistical differences were assessed using one-way ANOVA with Tukey post-test. *p<0.05, ***p<0.001, ****p<0.0001. (MP=micron sized HA; BMnP=bone mimetic nano particles)

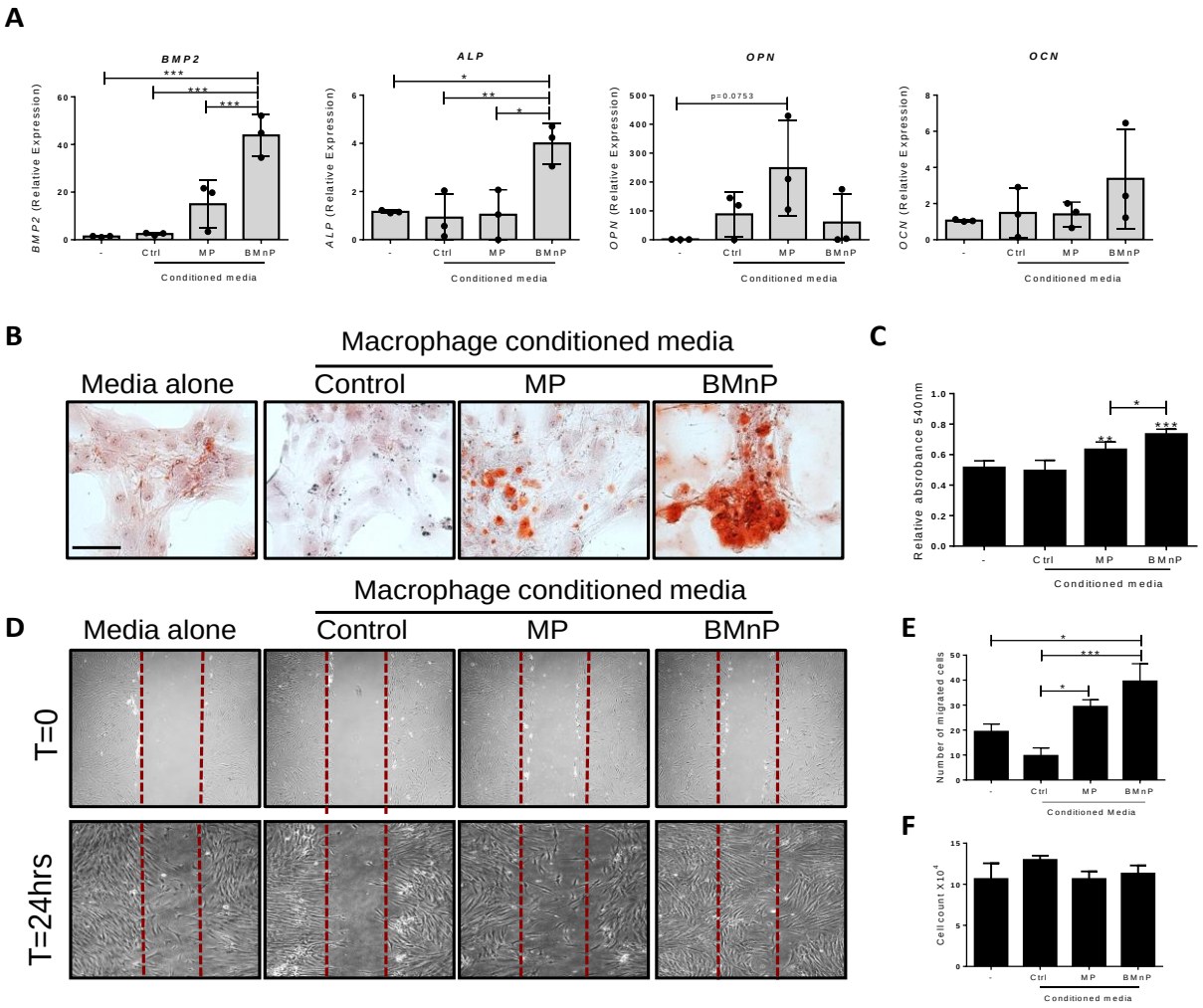

Fig. 3. Conditioned media from nanoparticle treated macrophages enhances osteogenic differentiation and MSC migration. (A) Human MSCs (1x 10^5 cells/ml) were cultured in media alone or conditioned media from untreated, micron or nano particle treated macrophages for 48 hours. mRNA levels of BMP2, ALP, Osteopontin or Osteocalcin were analyzed by qRT-PCR. Results shown are means (+/-SEM) for triplicate cultures of 3 independent experiments. Statistical differences were assessed using Kruskal Wallis test with Dunn's post-test, *p<0.05, **p<0.01, ***p<0.001. **(B)** Human MSCs were treated as above before being cultured for a further 7 days in osteogenic media assess downstream mineralization and calcification. Cells were then stained with

AR and imaged under an inverted microscope. Magnification =20x. Scale bar = 50µm. **(C)** Cells were destained using 10% cetylpyridinium chloride and AR dye was quantified by measuring absorbance at 540 nm. **(D)** Representative images of human MSC migration following culture in media alone or conditioned media from untreated, MP or BMnP treated macrophages. **(E)** Cells were counted by blinded individuals at 6 pre-determined imaged sites from each healthy donor and a mean value per donor was calculated and plotted. Results shown are mean (+/- SEM) and are representative of 3 independent experiments. **(F)** Cell count of MSCs after 48 hours in macrophage conditioned media. Results shown are mean (+/- SEM) and are representative of 3 independent experiments. Statistical differences were assessed using one-way ANOVA with Tukey post-test, *$p<0.05$, **$p<0.01$, ***$p<0.001$ versus media alone control. (MP=micron sized HA; BMnP=bone mimetic nano particles)

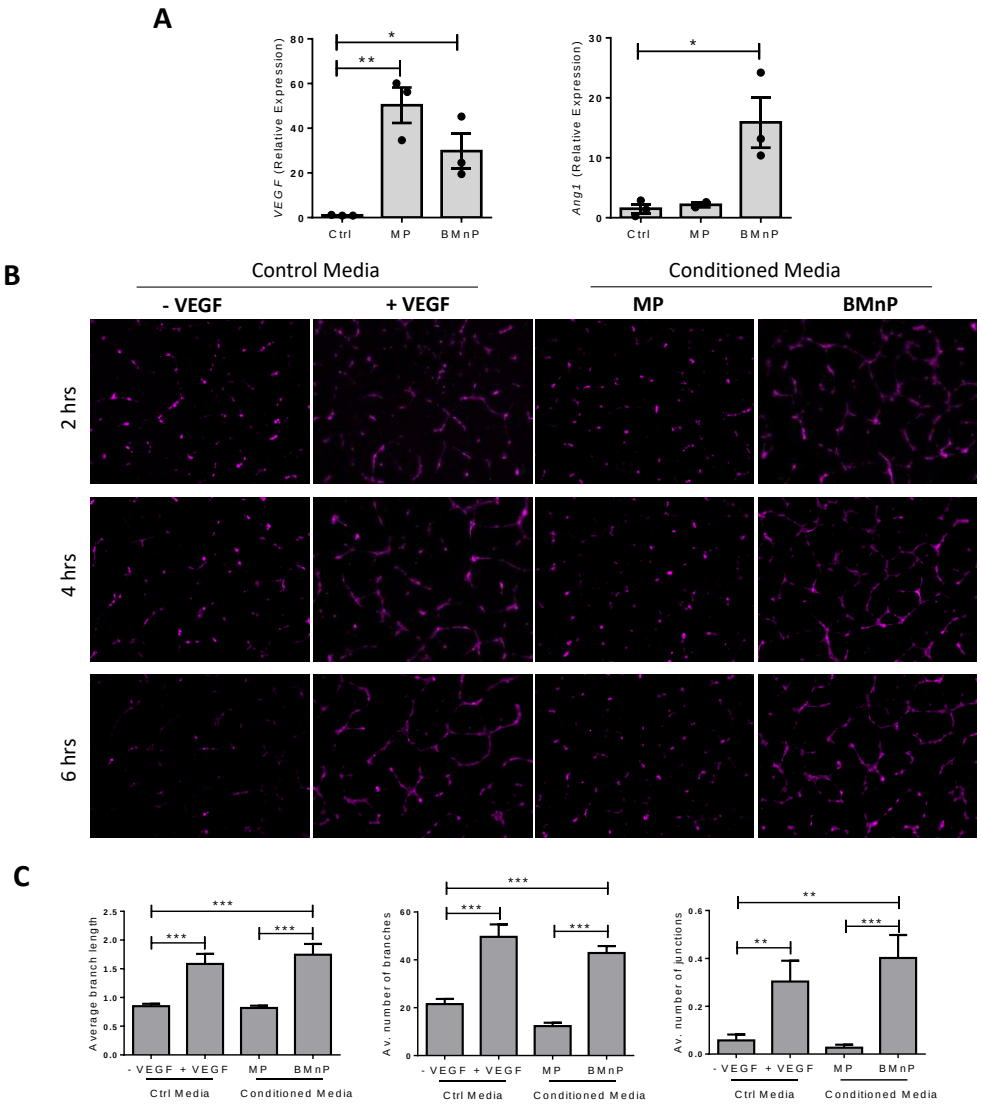

Fig. 4. Nanoparticles drive pro-angiogenic responses in human macrophages and HUVECs **(A)** Primary human macrophages (1x 10^6 cells/ml) were stimulated with micron or nano particles (250µg/ml) for 24 hours. mRNA levels of VEGF and Ang1 were analyzed by qRT-PCR. Results shown are means (+/- SEM) for triplicate cultures of 3 independent donors. **(B)** HUVECs (2 x 10^4) were seeded onto Matrigel coated plates in serum-free control media (EGM-2MV) without or with VEGF (10 ng/ml) as negative and positive controls respectively. Alternatively, cells were seeded in 50% supplemented serum-free conditioned media from micron or nano particle treated

macrophages. Cells were imaged using phase-contrast microscopy every 2 hours to assess endothelial cell tubule formation. **(C)** Average branch length, average number of branches and average number of junctions were quantified using ImageJ. Statistical differences were assessed using one-way ANOVA with Tukey post-test. **$p<0.01$, ***$p<0.001$. (MP=micron sized HA; BMnP=bone mimetic nano particles)

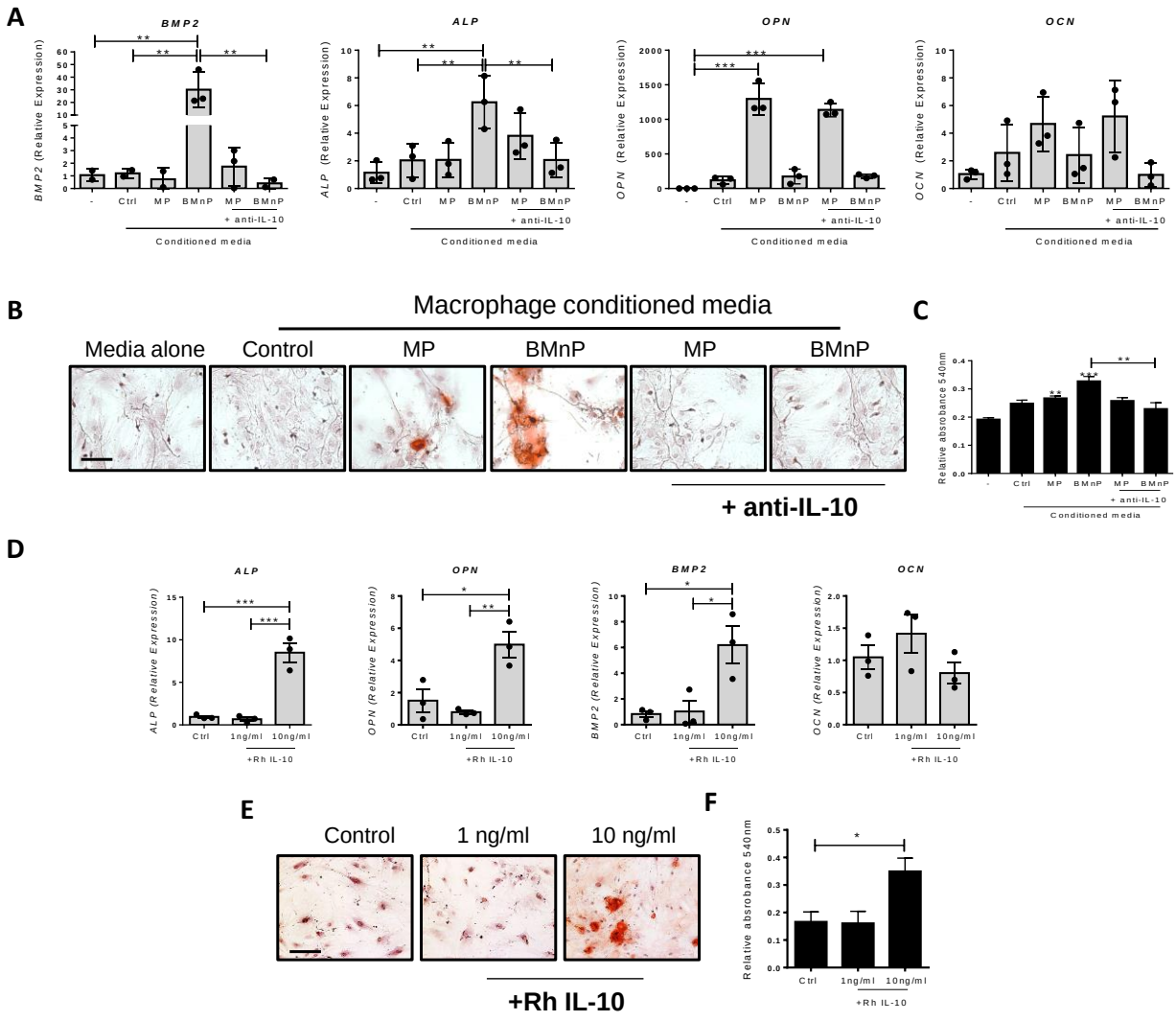

Fig. 5. Conditioned media from nanoparticle treated macrophages drives osteogenesis and mineralization of human MSCs in an IL-10 dependent manner. (A) Human MSCs (1x 10^5 cells/ml) were cultured in media alone or conditioned media from untreated, micron or nano particle treated (+/- pre-treatment with an IL-10 neutralizing antibody (2 µg/ml)) macrophages for 48 hours. mRNA levels of BMP2, ALP, OPN or OCN were analyzed by qRT-PCR. Results shown are means (+/-SEM) for triplicate cultures of 3 independent experiments. Statistical differences were assessed using Kruskal Wallis test with Dunn's post-test, *p<0.05, **p<0.01, ***p<0.001. **(B)** Human MSCs were treated as above before being cultured for a further 7 days in osteogenic

media to look at downstream mineralization and calcification. Cells were then stained with AR and imaged under an inverted microscope. Magnification =20x, Scale bar = 50µm **(C)** Cells were destained using 10% cetylpyridinium chloride and AR dye was quantified by measuring absorbance at 540nm. Results shown are mean +/-and are representative of 3 independent experiments. Statistical differences were assessed using one-way ANOVA with Tukey post-test, *p<0.05, **p<0.01, ***p<0.001 versus media alone control. **(D)** Human MSCs (1x 10^5 cells/ml) were treated with recombinant human (Rh) IL-10 (1ng/ml or 10ng/ml) for 48 hours and mRNA levels of ALP, Osteopontin, BMP2 and OCN were analyzed by qRT-PCR. Statistical differences were assessed using one-way ANOVA with Tukey post-test, *p<0.05, **p<0.01, ***p<0.001 versus untreated control. **(E)** Standard expansion media for human MSCs was supplemented with Rh IL-10 (1ng/ml or 10ng/ml) and calcification as assessed by AR staining was measured at day 7. Magnification = 20 x, Scale bar = 50µm. **(F)** Cells were destained using 10% cetylpyridinium chloride and AR dye was quantified by measuring absorbance at 540 nm. Statistical differences were assessed using one-way ANOVA with Tukey post-test, *p<0.05, versus untreated control. (MP=micron sized HA; BMnP=bone mimetic nano particles)

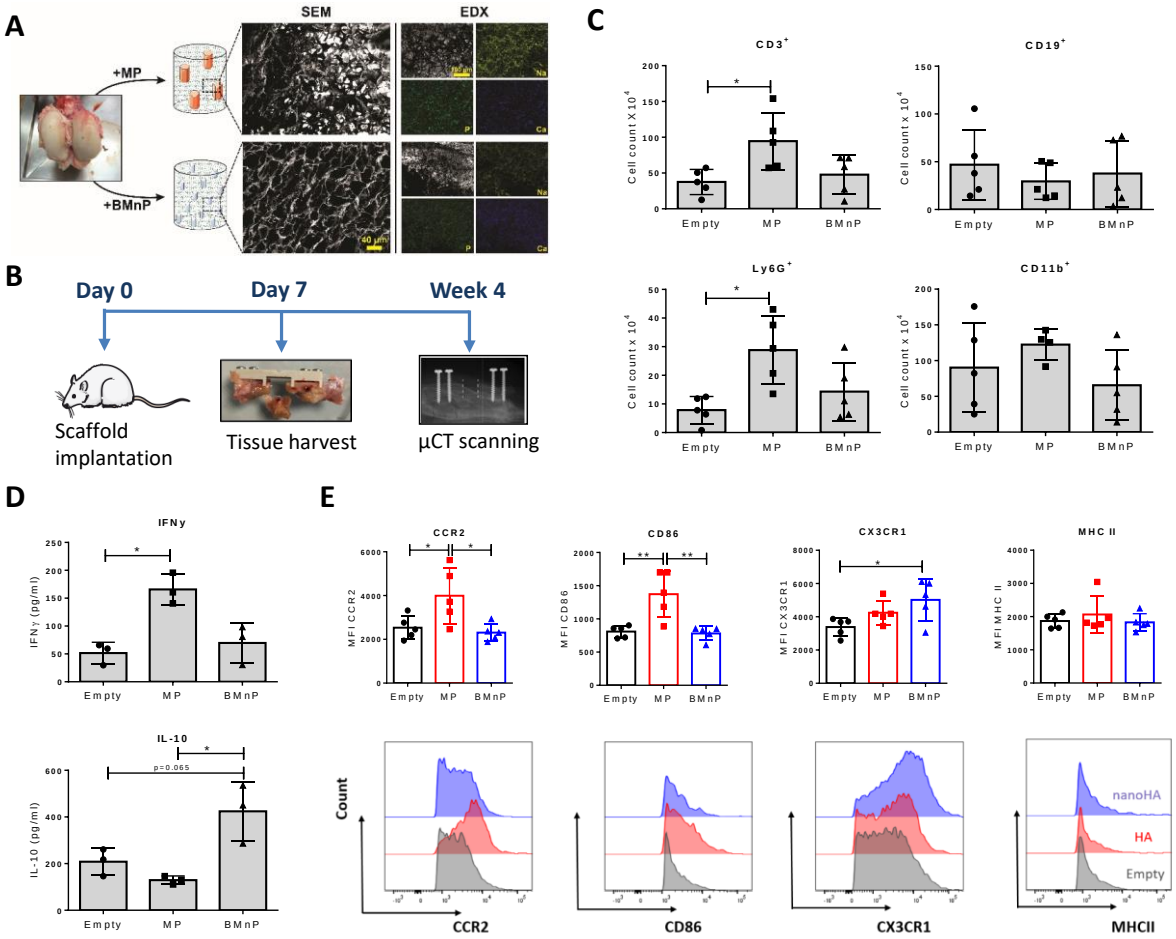

Fig. 6. Characterization of immune cell subsets and phenotype following implantation of hydroxyapatite functionalized scaffolds into a rat femoral defect model. (A) Schematic depicting micron HA or BMnP functionalized scaffold preparation using ECM material derived from porcine articular cartilage (AC). Representative SEM and EDX images depicting scaffold architecture and element composition. **(B)** Surgical model schematic. **(C)** Flow cytometric analysis of immune cell subsets within the defect site 1 week after implantation. **(D)** Cardiac punctures were performed and serum was isolated from blood samples. IL-10 and IFNγ cytokine levels were by ELISA. **(E)** Analysis of macrophage population at defect site expressing CCR2, CD86, CX3CR1 and MHCII with representative histograms of each marker. Statistical differences on n=5

rats were assessed using Kruskal Wallis test with Dunn's post-test, *p<0.05, **p<0.01. (MP=micron sized HA; BMnP=bone mimetic nano particles)

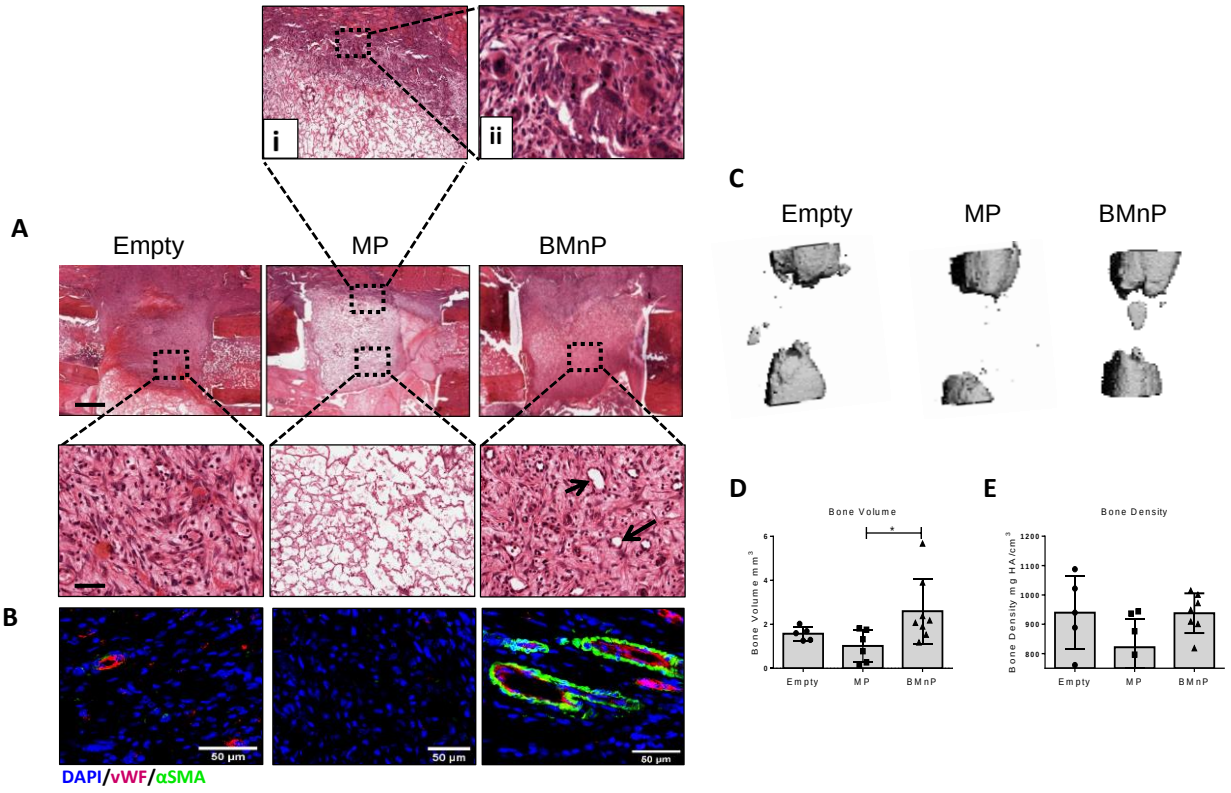

Fig. 7. Nanoparticle functionalized scaffolds accelerate bone tissue repair following implantation into a rat femoral defect model. (A) Representative images of low magnification H & E stained tissue at the defect site 1 week post implantation. Images taken at 2 x (upper panel, scale-bar 1 mm) and 10 x (lower panel, scale-bar 200 µm). Arrows indicate the presence of vessel like structures. High magnification of H & E stained samples showing fibrous encapsulation (i) and multinucleated cell formation (ii) **(B)** Representative images of vessel formation 1 week post implantation. von Willibrand factor (vWF) shown in red, α-SMA in shown in green and DAPI in

blue. Scale bar = 50 μm. **(C)** Reconstructed in vivo μCT analysis of bone formation at the defect site at 4 weeks. **(D)** Graphs represent quantification of total bone volume (mm^3) and **(E)** average bone density (mg HA/cm^3) at the defect site. Statistical differences (n=7 rats) were assessed using Kruskal Wallis test with Dunn's post-test, *$p<0.05$. (MP=micron sized HA; BMnP=bone mimetic nano particles)

Supplementary Figures

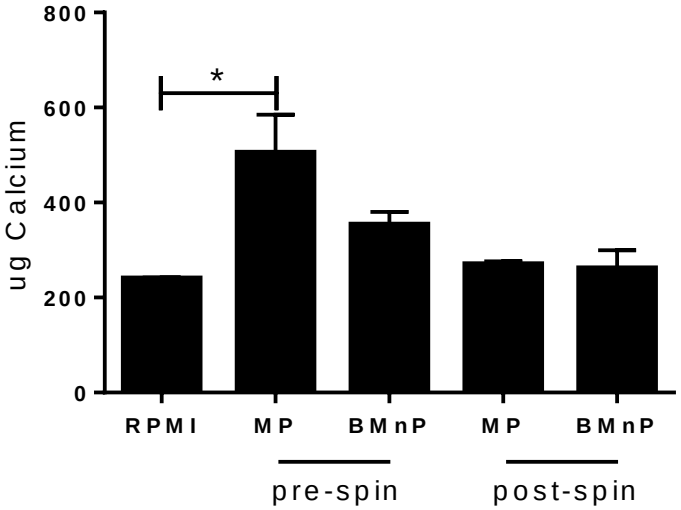

Fig. S1. Analysis of calcium content in conditioned media pre and post centrifugation. Calcium content in media pre- and post-centrifugation was determined using the o-cresolphthalein complexone (oCPC) method where a violet colored complex is formed between calcium ions reacting with oCPC[246] (Sentinel Diagnostics). *p<0.05 vs RPMI alone. (MP=micron sized HA; BMnP=bone mimetic nano particles)

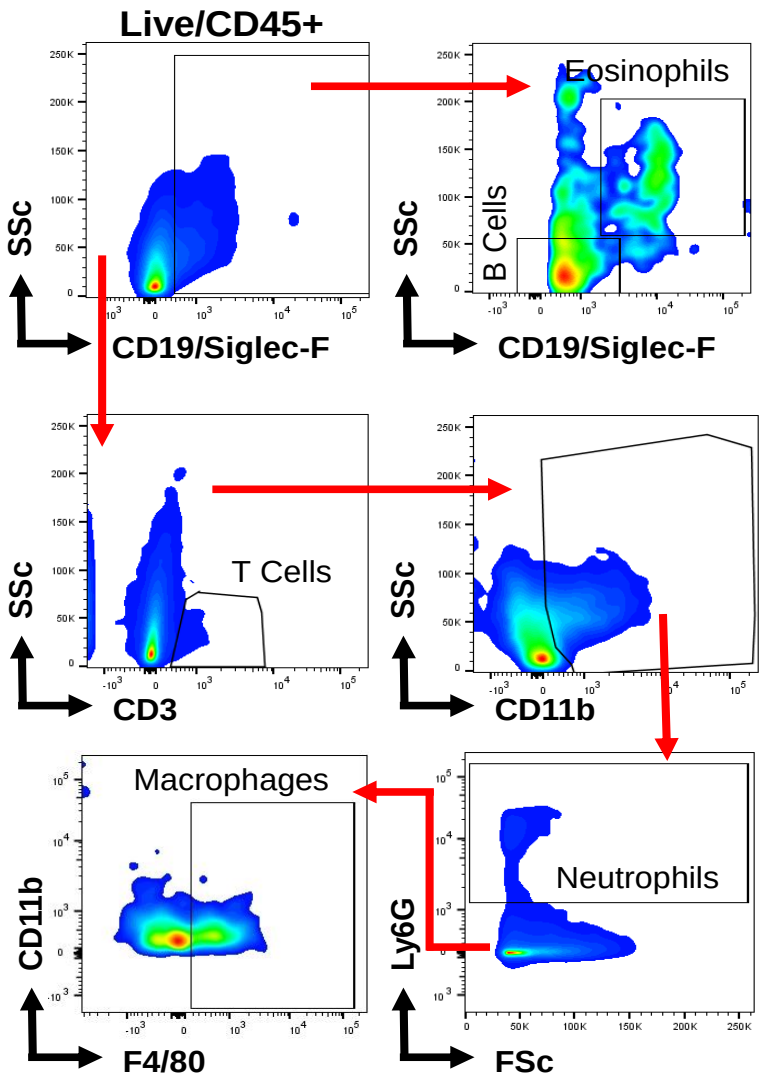

Fig. S2. Gating strategy for immune cell populations. Cells generated by digest of the tissue were antibody stained and analyzed by flow cytometry. Firstly, live/CD45+ immune cells were selected and basophils and eosinophils were gated on based on CD19/Siglec F expression. T cells were then selected for on the basis of their SSC area and CD3 expression. Total CD11b population was gated on and neutrophils were selected on their LY6G expression. Finally, CD11b/F4/80 double positive cells were selected as the macrophage population.

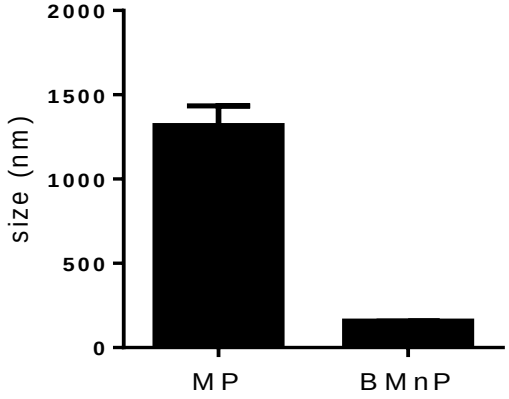

Fig. S3. Analysis of particles size. Particle size distribution using Dynamic Light Scattering (DLS). (MP=micron sized HA; BMnP=bone mimetic nano particles)

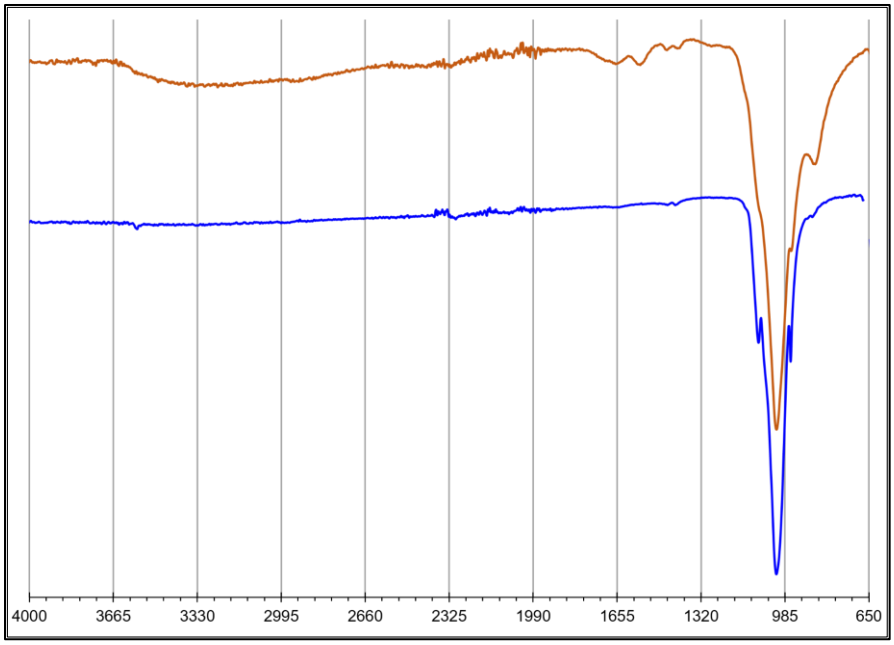

Fig. S4. Fourier-transform infrared (FTIR) spectra of nano (orange line) and micron (blue line) Hydroxyapatite particles.

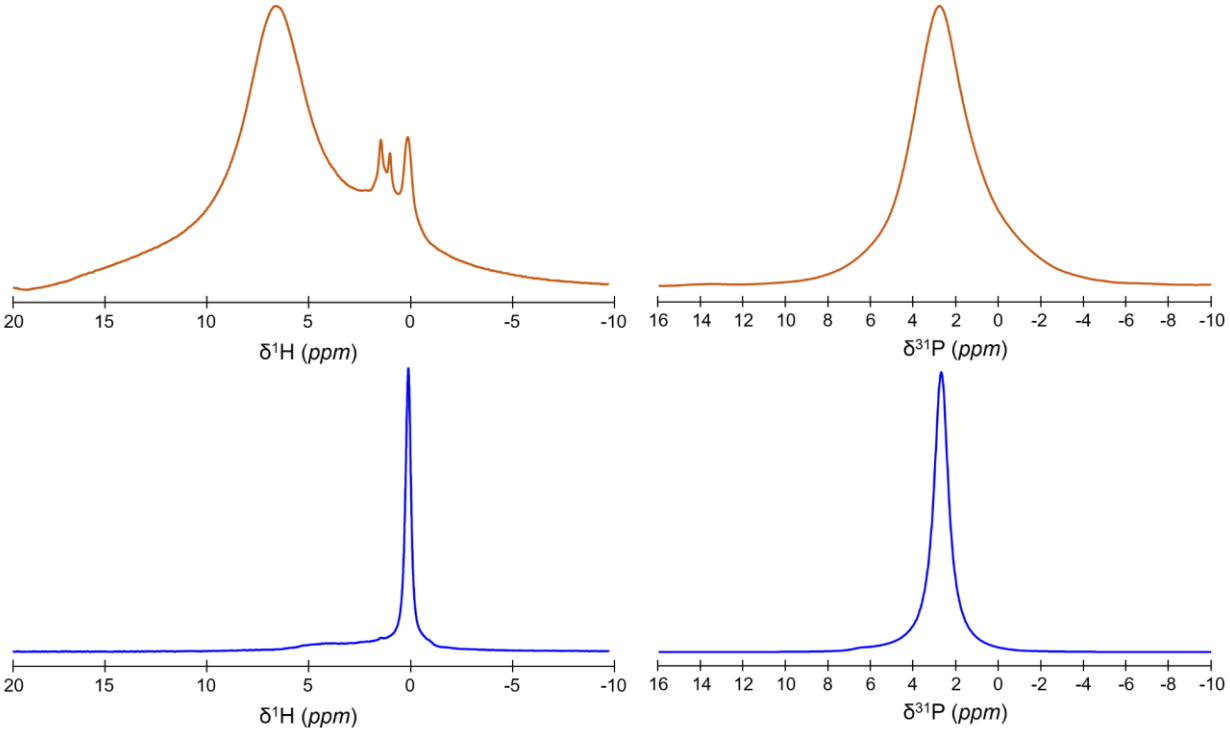

Fig. S5. One dimensional (1D) ^{1}H (left) and ^{31}P (right) single-pulse (SP) magic angle spinning (MAS) solid-state Nuclear Magnetic Resonance (NMR) spectra of nano (orange lines) and micron (blue lines) Hydroxyapatite particles.

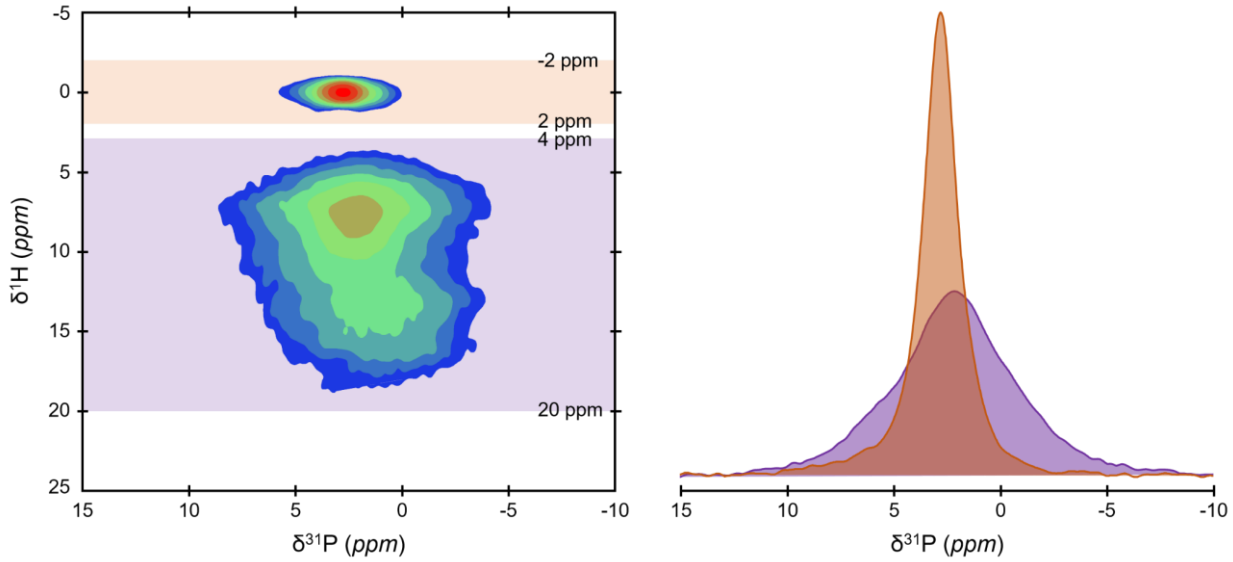

Fig. S6. One-dimensional (1D) individual ^{31}P NMR signals of the apatitic crystalline core (orange spectrum) and the amorphous surface layer (violet spectrum) of the nanoparticles. These individual ^{31}P NMR signals were extracted from the two-dimensional (2D) $\{^{1}H\}^{31}P$ Heteronuclear Correlation (HetCor) MAS NMR spectrum of nanoparticles that is shown here. To do this, the sums of the F2 slices taken at the OH^- ions position (orange area, from δ^1H = -2 to 2 ppm) in F1 have been used to generate the individual ^{31}P signal of the crystalline nanoparticle core. In addition, the sums of the F2 slices taken at the structural water molecules together with HPO_4^{2-} ions position (violet area, from δ^1H = 4 to 20 ppm) in F1 have been used to generate the individual ^{31}P signal of the amorphous surface layer.

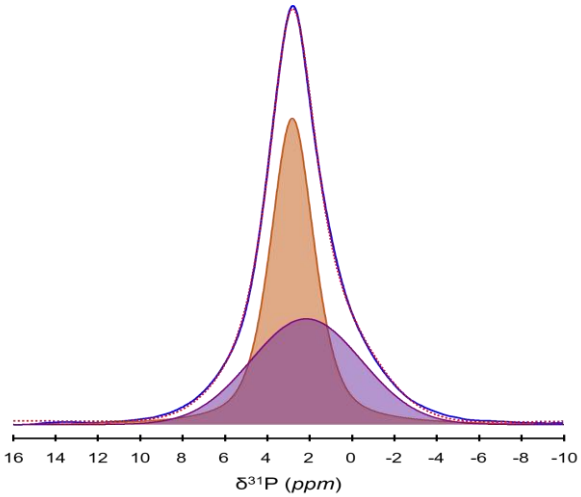

Fig. S7. Quantification of the molar proportion of HPO_4^{2-} and PO_4^{3-} ions respectively present in the amorphous surface layer and in the apatitic crystalline core of the nanoparticles. Here is shown a quantitative ^{31}P single-pulse (SP) magic angle spinning (MAS) solid-state Nuclear Magnetic Resonance (NMR) spectrum of nanoparticles (blue line) and its corresponding fitting (red dashed line) with two peaks. Those two peaks, whose lineshape and linewidth were revealed in Fig. S6, correspond to the PO_4^{3-}-containing apatitic crystalline core (orange peak) and the HPO_4^{2-}-containing amorphous surface layer (purple peak).

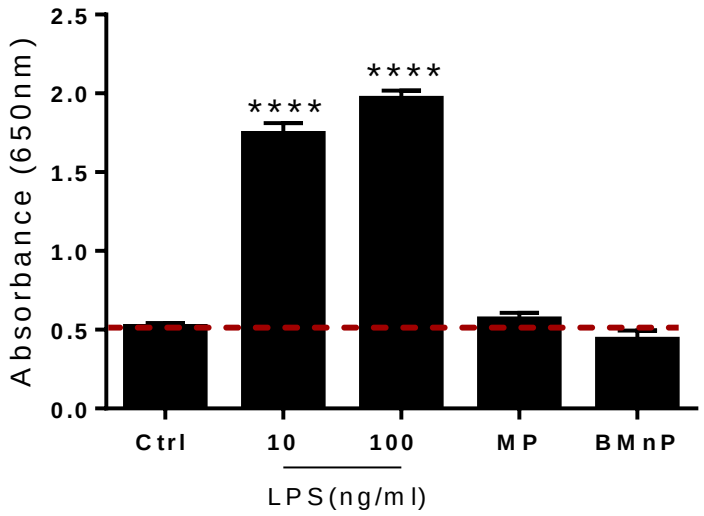

Fig. S8. Analysis of endotoxin levels. Both micron and nano Hydroxyapatite particle preparations were shown to be endotoxin free, using the HEK-Blue^{TM} hTLR4 assay system (Invivogen). The expression of SEAP, as measured by absorbance at 650nm, by particle treated macrophages was comparable to untreated control cells. As a positive control, cells were treated with LPS (10 ng/ml or 100 ng/ml). ****$p<0.0001$ vs untreated control. (MP=micron sized HA; BMnP=bone mimetic nano particles)

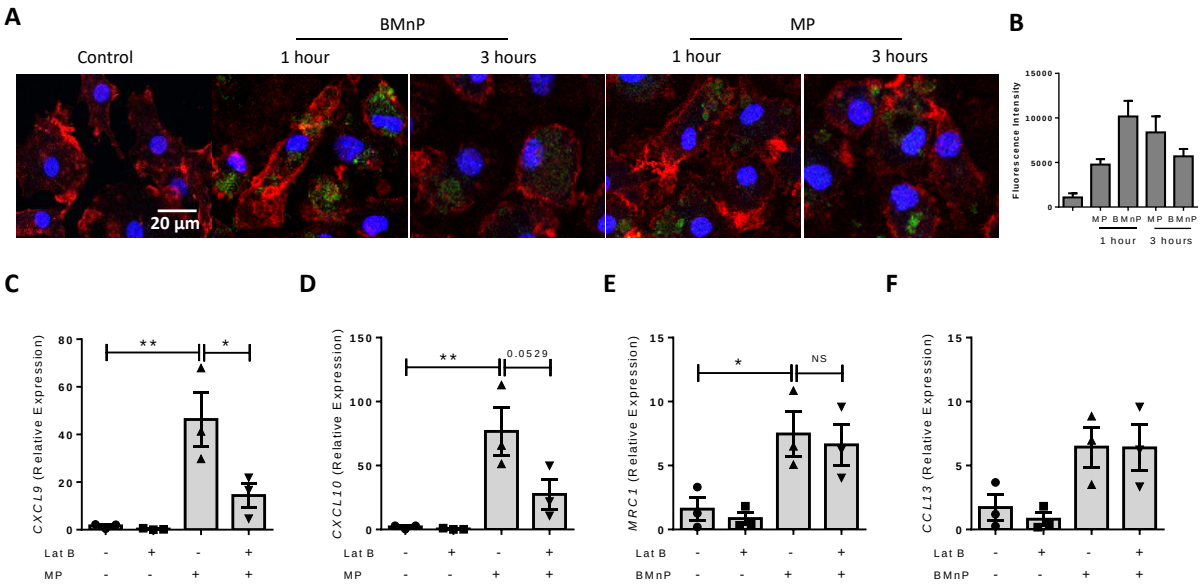

Fig. S9. Cellular uptake of fluorescently tagged particles by primary human macrophages. **(A)** Primary human macrophages (1x 10^6 cells/ml) were stimulated with FITC (green) tagged micron or nano particles (250 µg/ml) for 1 or 3 hours. Cells were fixed with PFA, and with rhodamine red to stain F-actin and DAPI to stain nuclei. Magnification =40x Scale bar = 20 µm. **(B)** FITC fluorescence quantification from images was assessed using Image J and is displayed as corrected total cell fluorescence (CTCF). **(C-F)** Primary human macrophages (1 x 10^6) were treated with micron or nano particles (250 µg/ml) alone or were pre-treated with the actin polymerization inhibitor, Latrunculin B (1 µM), prior to treatment with micron **(C & D)** or nano particles **(E & F)** for 24 hours. mRNA levels of the M1 genes CXCL9 and CXCL10 **(C & D)**, and the M2 genes **(E & F)** MRC1 and CCL13 were analyzed by qRT-PCR. Results shown are means (+/-SEM) for triplicate cultures of 3 independent experiments. Statistical differences were assessed using one-way ANOVA with Tukey post-test. *p<0.05, **p<0.01. (MP=micron sized HA; BMnP=bone mimetic nano particles)

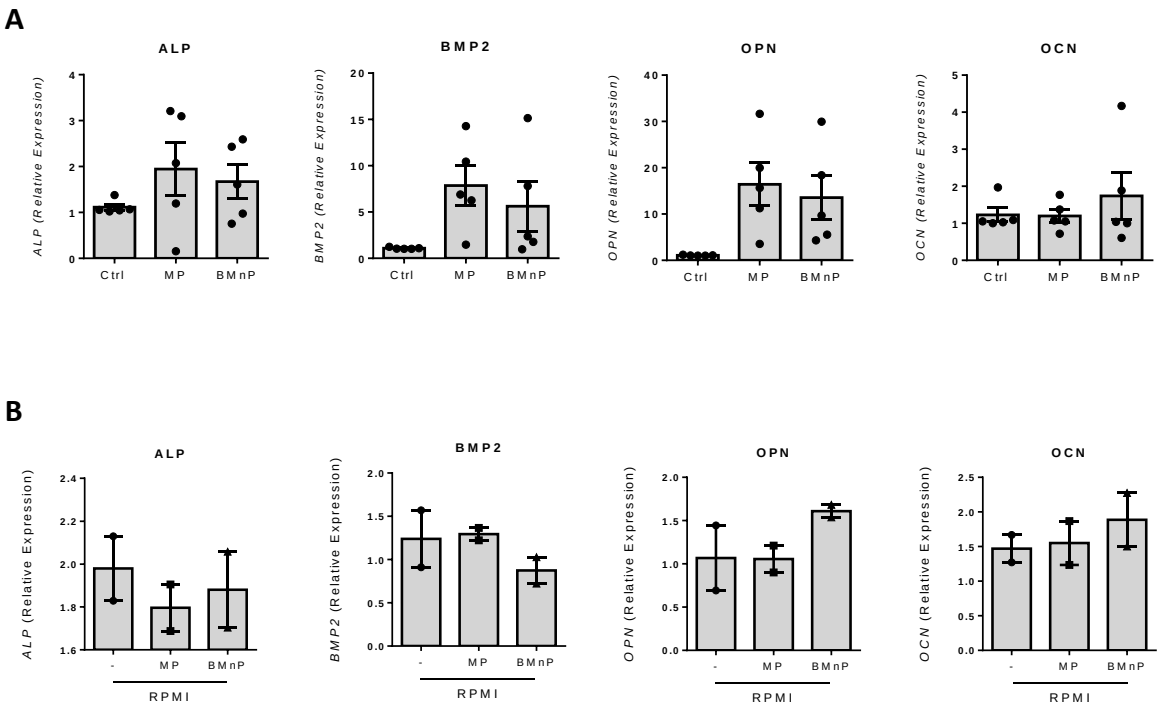

Fig. S10. Direct effect of particles or material release on MSC osteogenesis. (A) Human MSCs (1x 10^5 cells/ml) were left untreated or stimulated with micron or nano particles directly for 48 hours. mRNA levels of ALP, BMP2, OPN and OCN were analyzed by qRT-PCR. **(B)** Human MSCs (1x 10^5 cells/ml) were cultured in media alone or particle conditioned media for 48 hours. mRNA levels of ALP, BMP2, OPN and OCN were analyzed by qRT-PCR. Statistical differences were assessed using one-way ANOVA with Tukey post-test. (MP=micron sized HA; BMnP=bone mimetic nano particles)

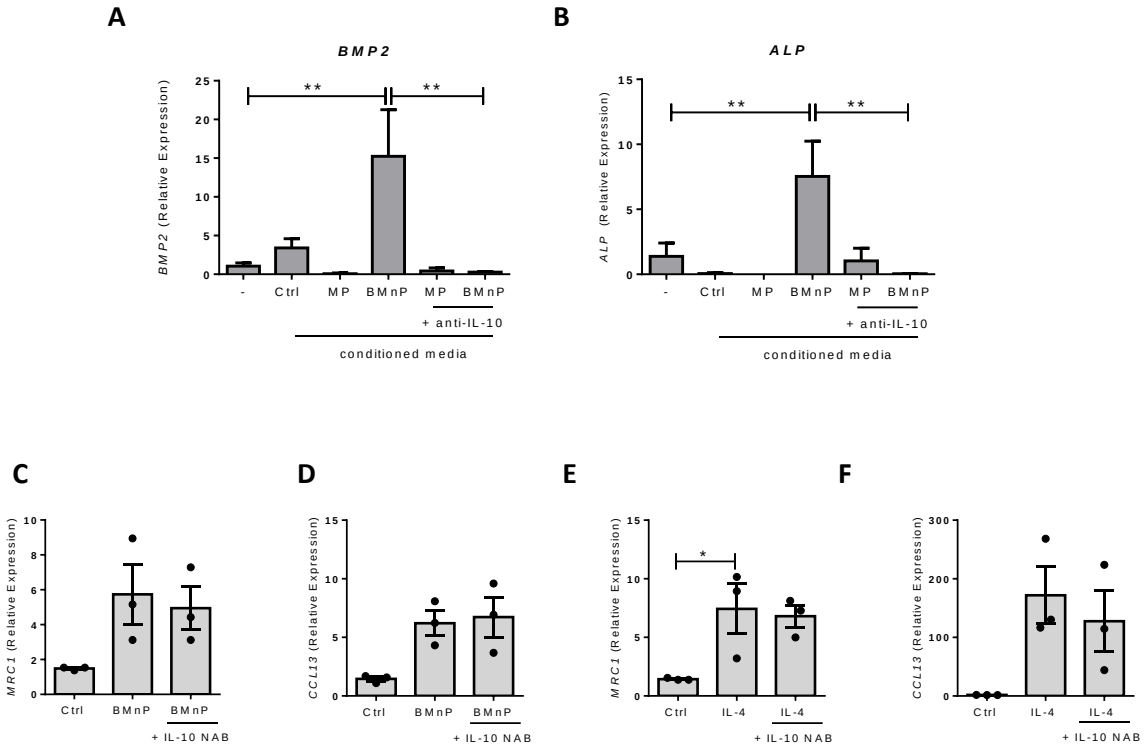

Fig. S11. The effect of IL-10 neutralization on M2 macrophage polarization. (A & B) Conditioned media from untreated, micron or nano particle treated macrophages was collected and incubated with an IL-10 neutralizing antibody (2 µg/ml) for 30 minutes at 37°C**.** Human MSCs (1x 10^5 cells/ml) were cultured in media alone or this conditioned media for 48 hours. mRNA levels of BMP2 and ALP were analyzed by qRT-PCR. **(C-F)** Primary human macrophages (1x 10^6 cells/ml) were stimulated with nano particles alone or in the presence of an IL-10 neutralizing antibody (2 µg/mL) for 24 hours. mRNA levels of **(C)** MRC1 or **(D)** CCL13 were analyzed by qRT-PCR. As an alternative M2 polarizing stimulus, cells were stimulated with IL-4 (20 ng/ml) alone or in the presence of an IL-10 neutralizing antibody (2 µg/mL) for 24 hours. mRNA levels of **(E)** MRC1 or **(F)** CCL13 were analyzed by qRT-PCR. Results shown are means (+/-SEM) for

triplicate cultures of 3 independent experiments. Statistical differences were assessed using one-way ANOVA with Tukey post-test. *p<0.05. (BMnP=bone mimetic nano particles)

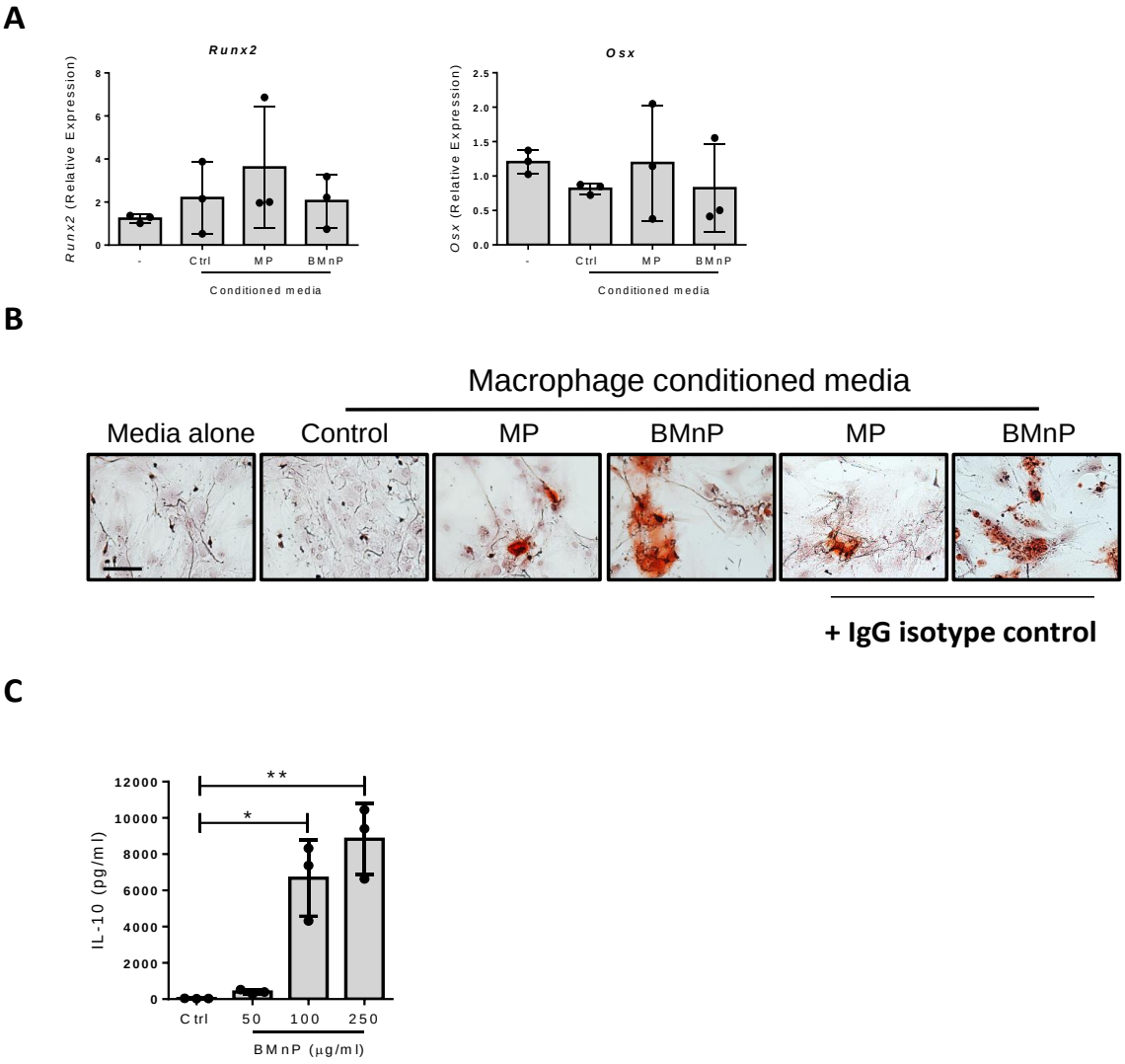

Fig. S12. Effect of conditioned media on osteogenic differentiation of MSCs. (A) Human MSCs (1x 10^5 cells/ml) were cultured in media alone or conditioned media from untreated, micron or nano particle treated macrophages for 48 hours. mRNA levels of Runx2 and OSX were analyzed by qRT-PCR. **(B)** Human MSCs (1x 10^5 cells/ml) were cultured in media alone or conditioned

media from untreated, micron or nano particle treated (+/- pre-treatment with an IgG isotype control antibody) macrophages for 48 hours before being cultured for a further 7 days in osteogenic media assess downstream mineralization and calcification. Cells were then stained with Alizarin red (AR) and imaged under an inverted microscope. Magnification =20x Scale bar = 50 µm. **(C)** IL-10 cytokine production from primary human macrophages stimulated with 50, 100 or 250 µg/ml) of nanoparticles. Results shown are means (+/-SEM) for triplicate cultures of 3 independent experiments. Statistical differences were assessed using one-way ANOVA with Tukey post-test. *$p<0.05$, **$p<0.01$. (MP=micron sized HA; BMnP=bone mimetic nano particles)

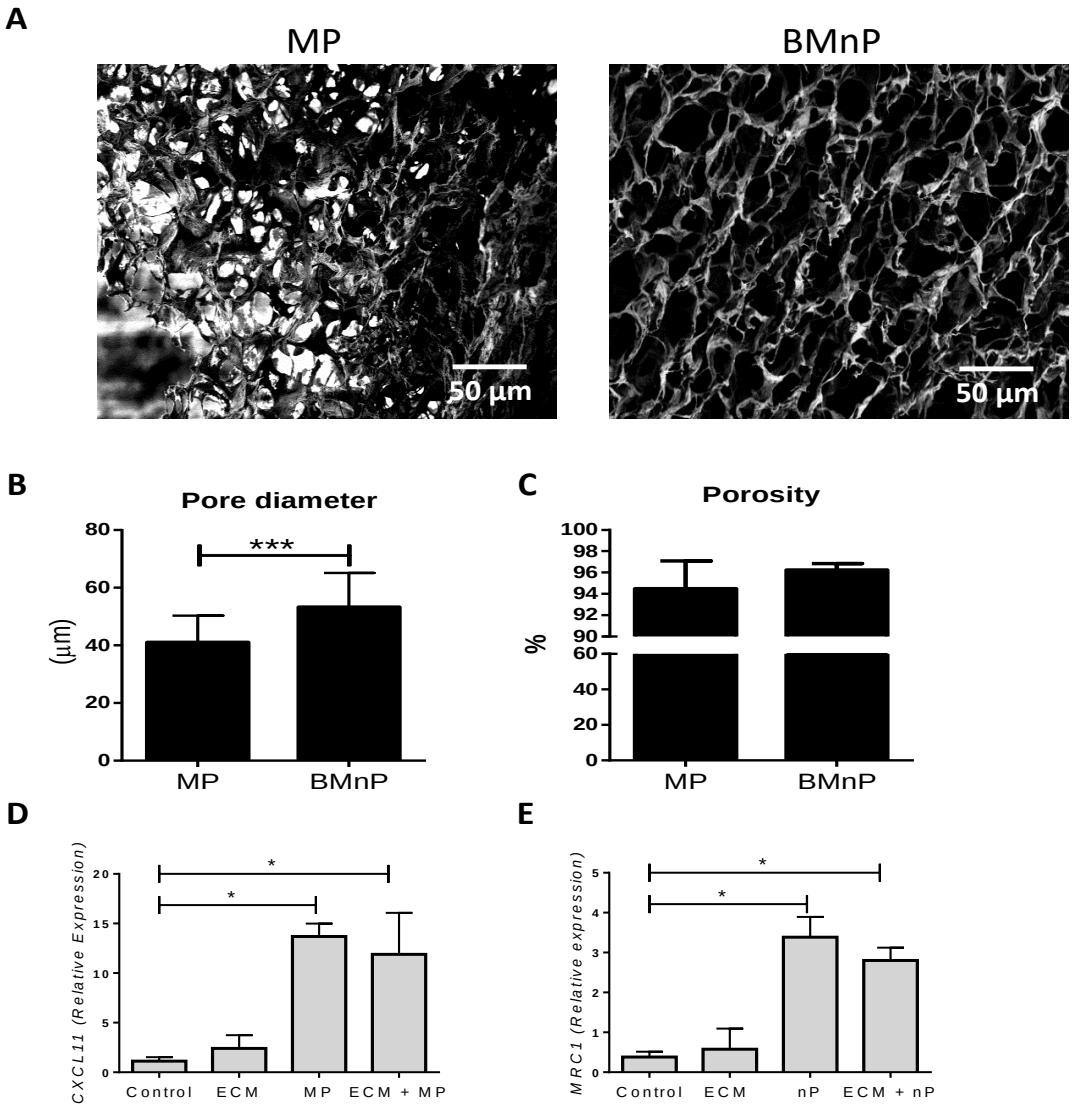

Fig. S13. Fabrication of MP and BMnP functionalized scaffolds. **(A)** SEM images of MP or BMnP functionalised ECM scaffolds. **(B)** Scaffold pore size after functionalization was measured using Image J software. **(C)** Scaffold porosity determined by gravimetry. **(D & E)** Primary human macrophages (1x 10^6 cells/ml) were stimulated with micron or nano particle functionalized ECM scaffolds for 24 hours. mRNA levels of CXCL11 and MRC1 were analyzed by qRT-PCR. Statistical differences were assessed using one-way ANOVA with Tukey post-test, *$p<0.05$,

**p<0.01, ***p<0.001 versus media alone control. (MP=micron sized HA; BMnP=bone mimetic nano particles)

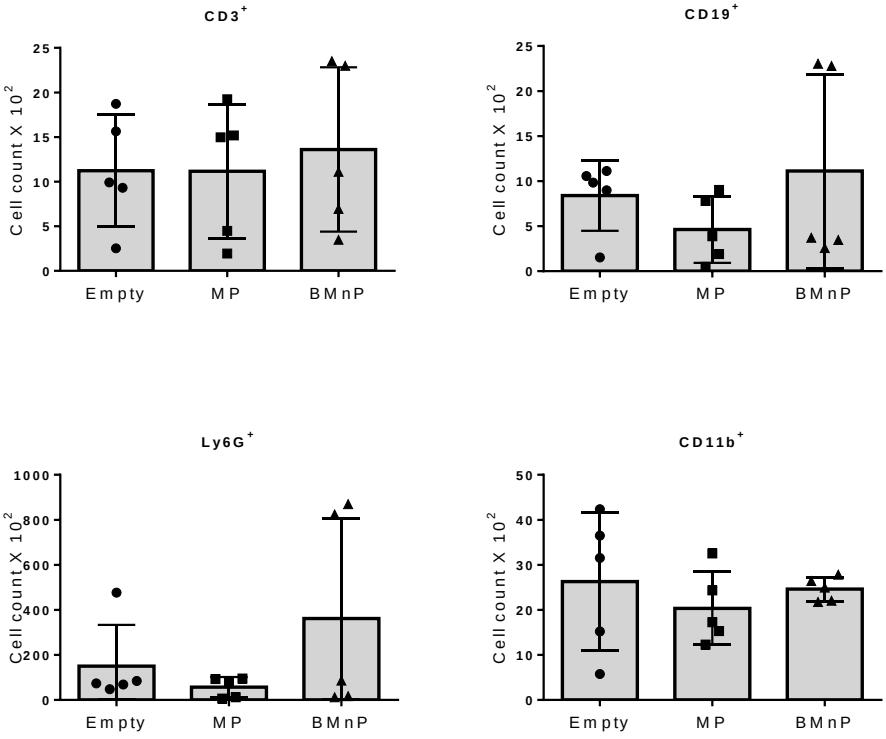

Fig. S14. Flow cytometric analysis of immune cell subsets outside the defect site 1 week after implantation. Outer tissue surrounding the defect site was isolated and digested. $CD3^+$ T cells, CD19+ B cells, $Ly6G^+$ neutrophils and $CD11b^+$/F4/80 macrophages were identified by flow cytometry. Statistical differences on n=5 rats were assessed using Kruskal Wallis test with Dunn's post-test. (MP=micron sized HA; BMnP=bone mimetic nano particles)

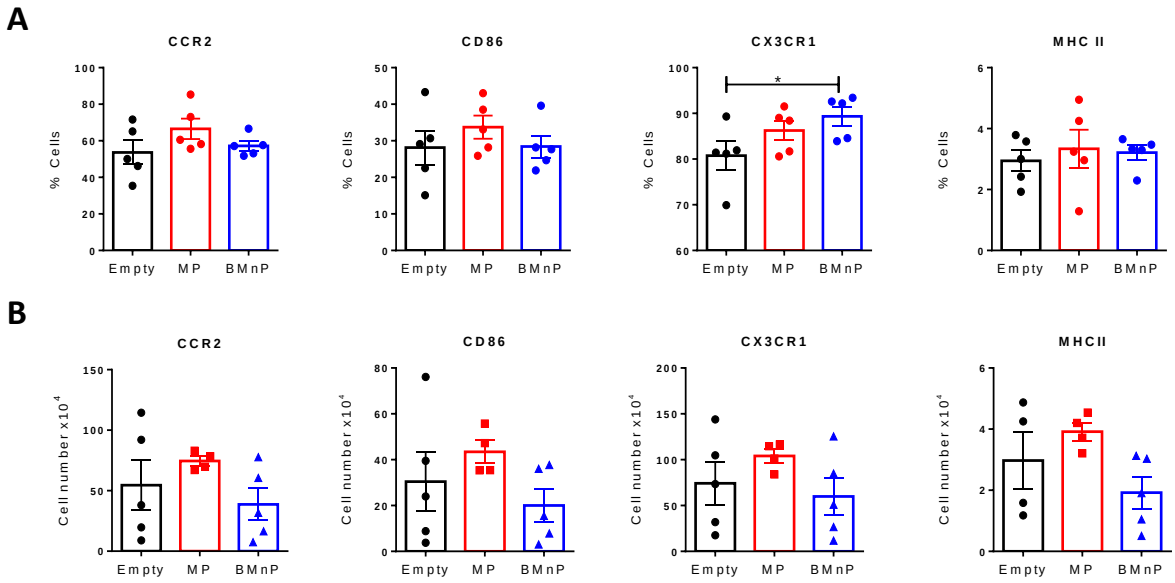

Fig. S15: Characterization of macrophage phenotype following implantation of hydroxyapatite functionalized scaffolds into a rat femoral defect model. HA or BMnP functionalised scaffolds were implanted into a 5mm rat femoral defect, or defect was left empty with no implant as a control. Tissue was harvested 1 week post implantation, digested and macrophage populations at defect site were analysed by flow cytometry. Macrophages were gated as F4/80+/CD11b+ and their phenotype assessed by surface marker expression. **(A)** Percentages of macrophages expressing CCR2, CD86, CX3CR1 and MHCII. **(B)** Absolute number of CCR2, CD86, CX3CR1 and MHCII positive cells at defect site. Statistical differences on n=5 rats were assessed using Kruskal Wallis test with Dunn's post-test, *p<0.05 (MP=micron sized HA; BMnP=bone mimetic nano particles)

Supplementary Materials

Table S1. Primer Sequences

Gene	Forward	Reverse
GAPDH	ACAGTTGCCATGTAGACC	TTTTTGGTTGAGCACAGG
BMP2	TCCACCATGAAGAATCTTTG	TAATTCGGTGATGGAAACTG
ALP	TCTTCACATTTGGTGGATAC	ATGGAGACATTCTCTCGTTC
OPN	GACCAAGGAAAACTCACTAC	CTGTTTAACTGGTATGGCAC
OCN	TTCTTTCCTCTTCCCCTTG	CCTCTTCTGGAGTTTATTTGG
Runx2	AAGCTTGATGACTCTAAACC	TCTGTAATCTGACTCTGTCC
Osx	TGAGGAGGAAGTTCACTATG	CATTAGTGCTTGTAAAGGGG
ANG1	TACTCAGTGGCTGCAAAAACTTGA	ATCTCCGACTTCATGTTTTCCACA
VEGF	GCAGAATCATCACGAAGTGGTG	TCTCGATTGGATGGCAGTAGCT

Table S2. Dilutions for Primary Antibodies

Antibody	Dilution
Anti-phospho-Stat-3	1:500
Anti-CD206	1:1000
Anti-CD163	1:1000
Anti-CD80	1:500
Anti-cMaf	1:300
Anti-β-actin peroxidase	1:50,000

Table S3. Antibodies for Flow Cytometry

Specificity	Clone	Flourochrome	Supplier
CD14	HCD14	FITC	eBioscience (San Diego, CA)
CD86	IT2.2	PerCP-e710	BioLegend (san Diego, CA)
CD163	GHI/61	BV421	BioLegend (san Diego, CA)
CD206	19.2	APC	eBioscience (San Diego,CA)
CD11b	M1/70	APC-Cy7	eBioscience (San Diego, CA)
CD45	30-F11	BV785	BioLegend (san Diego, CA)
CD3	17-A2	PE	eBioscience (San Diego, CA)
Ly6G	1A8	Pacific Blue	eBioscience (San Diego, CA)
CCR2	SA203G11	PE-Cy7	BioLegend (san Diego, CA)
CX3CR1	SA011F11	BV650	BioLegend (san Diego, CA)
Ly6C	AL-21	FITC	eBioscience (San Diego, CA)
Siglec F	E50-2440	PE-Dazzle	eBioscience (San Diego, CA)
MHCII	M5144.15.2	APC	BioLegend (san Diego, CA)
CD19	1D3	PE-Dazzle	eBioscience (San Diego, CA)
F4/80	BM8	PerCP-CY5.5	eBioscience (San Diego, CA)